This is the peer-reviewed, final accepted version for American Mineralogist, published by the Mineralogical Society of America.
The published version is subject to change. Cite as Authors (Year) Title. American Mineralogist, in press.
DOI: https://doi.org/10.2138/am-2023-9083. http://www.minsocam.org/

REVISION 1

The Effect of the ^{A}Na-^{A}K ratio on Chlorine Incorporation into Hastingsitic Amphiboles

Jared P. Matteucci[1*]

David M. Jenkins[1]

M. Darby Dyar[2]

[1]Dept. Earth Sciences

Binghamton University

Binghamton, NY 13902-6000

[2]Department of Astronomy

Mount Holyoke College

South Hadley, Massachusetts 01075-1429

*Corresponding author

Abstract

Chlorine-rich fluids play an important role in many geological processes, including the formation of economic deposits, crustal and mantle metasomatism, and high-grade metamorphism. Furthermore, the chlorine content of a fluid is often one of the main variables, dictating the fluid's properties (i.e., the propensity for mass transport). Calcium amphiboles have the potential to be used to determine the chlorinity of paleo fluids, given sufficient knowledge of

how Cl is partitioned between amphibole and fluid. Amphiboles with Fe# [= $Fe^{2+}/(Fe^{2+} + Mg)$] = 1.0 were synthesized along the hastingsite–potassic-hastingsite join in the presence of variably concentrated $FeCl_2$ brines, ranging from 1 molal to 100 molal. Syntheses were done at 700 °C and 3 kbar at fO_2 values near Ni-NiO for durations of 96-132 hours. All amphiboles were characterized by powder X-ray diffraction and electron microprobe and several samples were analyzed by Mössbauer spectroscopy to determine ferric iron content. Results showed that amphibole Cl content increased linearly with the mole fraction of Cl in the brine and has no obvious relationship with the K# (= K/(K+Na)). Amphibole Cl contents varied from ~0.05 atoms per formula unit (apfu), synthesized in the most dilute brines, to ~1.05 apfu, synthesized in the most concentrated brines. Amphibole yield was related to the K#, with higher amphibole yields for the more K-rich bulk compositions. The amphibole ferric iron fraction was dependent on the brine $FeCl_2$ concentration, increasing from 0.176 at 1 molal $FeCl_2$, to 0.310 at 24 molal $FeCl_2$. For brines more concentrated than 24 molal $FeCl_2$, the ferric iron fraction significantly decreased to 0.116 at 50 molal $FeCl_2$. The significant decrease in ferric iron fraction also coincided with a transition from magnetite to fayalite as a coexisting phase. The ferric iron fraction seemed to influence the total occupancy of the *A* site through the following reaction: $A^+ + Fe^{2+} \leftrightharpoons \square + Fe^{3+}$, where $\square$ is a vacancy. Trends between Fe^{3+} and Cl display both positive and negative correlations, raising further questions on the role of Fe^{3+} on Cl incorporation. The findings of this study indicate that for Fe# = 1.0 amphiboles, the Cl concentration of the fluid plays the dominant, or perhaps only, role in amphibole Cl incorporation, with the occupant of the *A* site being inconsequential.

Keywords: Hastingsite, *A*-site cation, $FeCl_2$ brine, Calcium amphibole, Chlorine content

Introduction

The halogen content of amphiboles can be a valuable tool for understanding the behavior of paleofluids, which have a direct role in several geologic processes, such as mantle and crustal metasomatism (Kusebauch et al., 2015; Frezzotti et al., 2010; Selverstone and Sharp, 2011), formation of ore deposits (Yardley and Bodnar, 2014), and the shifting of reaction boundaries involving H_2O (Aranovich and Newton, 1997). As noted by Yardley and Bodnar (2014), Cl is a "master variable" in aqueous geochemistry because its concentration is seldom constrained and often highly variable, controlling the total amount of dissolved cations.

The migration of aqueous fluids is the dominant process of mass transfer in the crust (Newton and Manning, 2010). Mass transfer via aqueous fluid flow is generally enhanced by Cl, largely due to the formation of complexes between metals and chlorine (Yardley and Graham, 2002). Therein exists the potential to use chloro-amphiboles to detect ancient Cl-rich brines, which could then be used to identify potential ore deposits. In addition to mass transport, dissolved chloride salts reduce the activity of H_2O in aqueous fluids and can thereby change the pressure-temperature (*P*-*T*) locations and slopes of chemical reactions involving H_2O. For example, the addition of KCl to water was shown by Chu et al. (2011) to significantly increase the solidus temperature of the forsterite-enstatite-water system by almost 400 °C at 50 kbar. In addition, Aranovich and Newton (1997) showed that the addition of chloride salts to the water-brucite-periclase system reduced brucite's breakdown temperature by 50 – 250 °C in the range of 1 – 15 kbar.

There is ample evidence from both field and experimental data that a Cl-rich amphibole cannot form unless it falls within a rather narrow compositional range. Jenkins (2019) found experimentally that amphiboles that are rich in K and Fe^{2+} are able to incorporate the most Cl and have compositions close to Fe-rich pargasitic and hastingsitic amphiboles with the general

composition $(K,Na)Ca_2(Fe^{2+}{}_4(Al,Fe^{3+}))(Al,Si)_8O_{22}(Cl,OH,O)_2$. The avoidance between Mg and Cl in amphiboles and micas has been extensively documented (e.g., Munoz, 1984; Morrison, 1991; Kullerud, 1996; Mueller et al., 2017). The K-Cl relationship is less clear; however, it is often observed that amphiboles with the highest total *A*-site cations have the highest amounts of Cl (e.g., Vanko, 1986; Enami et al., 1992). The ambiguity of the *A*-site-Cl relationship is illustrated in Liu et al., (2009), who documented Cl-rich amphiboles in the Yangkou eclogite of the Sulu metamorphic terrane in eastern China. Some of their amphibole analyses show a positive correlation between Na and Cl with no correlation between K and Cl, while others show a positive correlation between K and Cl and no correlation between Na and Cl.

Using chloro-amphiboles to quantify the composition of coexisting saline fluids requires an understanding of how Cl is partitioned between brine and amphibole. The only studies to date to address this are Chan et al. (2016) and Campanaro and Jenkins (2017), both of which studied the partitioning of Cl between NaCl brines and ferro-pargasite. Most of their experiments produced amphiboles with less than 0.1 atoms per formula unit (apfu) Cl. Their most Cl-rich amphibole had 0.64 apfu Cl, which was synthesized in a NaCl brine calculated at 126 m (molal).

This study is designed to explore Cl partitioning in more Cl-rich amphiboles, exceeding 1.0 apfu Cl. Iron (II) chloride was used as the source of Cl, which Chan et al. (2016) noted yielded more Cl-rich amphiboles (at constant brine Cl concentrations) compared to NaCl brines. A bulk composition equivalent to potassic-chloro-hastingsite $(KCa_2(Fe^{2+}{}_4Fe^{3+})(Al_2Si_6)O_{22}Cl_2)$ was used as it should provide a favorable crystal chemical environment for Cl incorporation (Jenkins, 2019). Furthermore, to explore the relationship between the *A*-site occupant and amphibole Cl content, a series of hastingsitic amphiboles were synthesized under constant brine Cl concentrations using different starting bulk compositions with the K# [$= (\frac{K}{K+Na})$] ranging from

1 (potassic-chloro-hastingsite) to 0 (chloro-hastingsite, $NaCa_2(Fe^{2+}_4Fe^{3+})(Al_2Si_6)O_{22}(OH,Cl)_2$). Varying amphibole K# under conditions of constant brine chlorinity will determine whether the amphibole's *A*-site occupant affects its ability to incorporate Cl into its structure, providing insight on both the crystal chemical and brine-Cl-concentration constraints to Cl incorporation into amphiboles.

Methods

Starting materials

Reagents used consisted of reagent-grade silicic acid hydrate ($SiO_2 \cdot xH_2O$, Alfa Aesar, reagent grade), aluminum oxide (Al_2O_3, Aldrich, 99.8%), ferric oxide (Fe_2O_3, Fisher, 99.8%), powdered metallic iron (~10 μm Fe°, Aldrich, 99.9+%), calcium carbonate ($CaCO_3$, J.T.Baker, 99.4%), sodium carbonate (Na_2CO_3, Fisher, >99.5%), potassium carbonate (K_2CO_3, Fisher, >99.0%), and ferrous chloride ($FeCl_2$, Aldrich, 98%). The silicic acid hydrate was heated in air to 1100 °C in a 1-atmosphere furnace to convert it into anhydrous silicon dioxide (mostly cristobalite). All reagents were stored in a desiccator filled with anhydrous calcium sulfate (Drierite). Amphibole equivalent mixtures were prepared by combining the reagents in proportion to their theoretical end-member bulk composition. The desired ratio of Fe_2O_3/FeO was achieved by mixing ferric oxide and fine-grained (~10 μm) metallic iron. All non-ferrous materials were combined, mixed under ethanol, and heated in a 900 °C furnace for 15 minutes to decarbonate the carbonate salts and partially vitrify the mixture, the latter to enhance its reactivity. The decarbonated mixture was weighed immediately upon cooling and the weight value was used to correct the amounts of the remaining ingredients needed. The Fe_2O_3 and Fe° were added next and homogenized under ethanol. The starting mixture as described to this point (excluding H_2O and $FeCl_2$) will be referred to as the oxide reagent, which has the volatile-free

composition of $(Na,K)Ca_2(Fe^{2+}{}_4Fe^{3+})(Al_2Si_6)O_{23}$. The iron (II) chloride and distilled water, which comprise the brine fraction of the starting material, were added later during the preparation of each individual charge in the correct proportions to achieve the desired $FeCl_2$ concentration with a brine/solid ratio of 0.20.

Sample preparation

One problem with using $FeCl_2$ as the source of Cl in a brine is its hygroscopic nature, absorbing water when in contact with a moist atmosphere. From X-ray diffraction (XRD) scans, the $FeCl_2$ reagent used in this study is not anhydrous and has some water absorbed in its structure and is better referred to as $FeCl_2{\cdot}nH_2O$. Since this study involves brines up to 100 molal $FeCl_2$, the system is sensitive to small amounts of water. The amount of water bound in $FeCl_2{\cdot}nH_2O$ can be as much as a few milligrams in a system with total mass near 50 mg. Although the solubility limit of $FeCl_2$ at the pressure (3 kbar) and temperature (700 °C) of this study is not known, it is assumed that the maximum brine concentration used here (100 m $FeCl_2$) is below saturation with respect to $FeCl_2$ as it has a similar solubility to that of NaCl (e.g., Weast et al., 1978), where the latter has a saturation limit of 83 m NaCl at these conditions (Driesner and Heinrich, 2007).

To quantify the amount of water present in the $FeCl_2{\cdot}nH_2O$ reagent, it was scanned with XRD each day a new charge was prepared. Because $FeCl_2$ is hygroscopic, scans were rapid (~ 5 min) to limit the absorption of atmospheric moisture, which allowed for a more accurate determination of the bound water in the reagent (molar mass of $FeCl_2{\cdot}nH_2O$, ± 3 $gmol^{-1}$) as it exists immediately after being removed from its storage bottle. Scans were from 12-70° 2θ with a time per step of 0.2 sec and a step size of 0.04°. The proportions of anhydrous $FeCl_2$, $FeCl_2{\cdot}2H_2O$, and $FeCl_2{\cdot}4H_2O$ were determined with Rietveld refinements, allowing for calculation of the molar mass of $FeCl_2{\cdot}nH_2O$. The hydration state of the $FeCl_2{\cdot}nH_2O$ was found

to be a function of the lab dew point (Figure 1) and its composition averaged near that of rokühnite ($FeCl_2 \cdot 2H_2O$).

To prepare a sample, about 50 mg of the oxide reagent was first measured out. Second, the amount of $FeCl_2 \cdot nH_2O$ to be added was calculated based on (i) the molar mass of $FeCl_2 \cdot nH_2O$ on that day, (ii) desired brine concentration, and (iii) desired brine/solid ratio of 0.20. After combining the oxide mixture and the $FeCl_2 \cdot nH_2O$, they were homogenized dry in an agate mortar and pestle for 10 minutes. This mixture was then added to a capsule made from welded $Ag_{50}Pd_{50}$ tubing with 4.0 mm outer-diameter (OD) and 0.13 mm wall thickness. The loaded capsule was heated in air to 160 °C for 15 minutes to drive away moisture absorbed by the $FeCl_2 \cdot nH_2O$ during homogenization. By comparing masses of the capsule before and after heating, it was found that the hydration state of the $FeCl_2 \cdot nH_2O$ returned to near its starting value as determined by XRD and was not fully dehydrated to anhydrous $FeCl_2$. By knowing the amount of oxide reagent and anhydrous $FeCl_2$ (which was calculated from the molar mass of $FeCl_2 \cdot nH_2O$), the amount of water present in the capsule after the initial heating at 160 °C in air could be determined. Finally, deionized water (DW, < 1 ppm Cl via ion chromatography) was added to the capsule (if necessary) to achieve the desired brine concentration of $FeCl_2$. For dilute brines, DW was added with a micro syringe, but for more concentrated brines, the capsule was just left open to air, slowly absorbing atmospheric water until the desired mass was reached.

The capsule was then crimped, and arc welded beneath a lightly moistened tissue to help reduce exposure of the AgPd melt to oxygen (Weidner 1989). During the welding procedure, the capsule was wrapped in a wet tissue to help reduce the amount of heat absorbed during welding which can potentially drive off some of the water in the mixture. The capsule was then weighed to ensure that mass (water) was not lost during welding.

After a run was complete, the capsule was weighed, punctured, weighed again, heated at 110 °C for 15 minutes, and weighed once more. Comparing the sealed weight of the capsule to the weight after puncture provides an indication of the quantity of any non-condensable volatiles. In addition, comparing this to the weight after heating provides an indication of the amount of water present in the capsule after treatment at *P* and *T*. However, as noted above, complete desiccation of the sample is difficult, so any mass loss produced via this method should be considered a minimum value.

Apparatus

The experiments were done in internally heated pressure vessels. Argon-hydrogen gas mixtures were used as the pressure medium. Treatment conditions were generally ~700° C and ~3 kbar with durations ranging from ~96 to ~136 hours. Two Inconel-sheathed chromel-alumel thermocouples were used to measure the thermal gradient along the length of the capsule during each experiment. The capsules were placed inside a hollow copper cylinder to reduce thermal gradients and to hold the samples in place near the thermocouple tips.

The f_{O_2} was controlled by establishing a partial pressure of hydrogen in the H_2-Ar gas mixture used as the pressure media in the internally heated pressure vessels. Using the activity coefficients (γ_{H_2}) of Shaw and Wones (1964), the hydrogen fugacity (f_{H_2}) was calculated from the H_2 partial pressure (P_{H_2}) in the H_2-Ar gas mixture as $f_{H_2} = \gamma_{H_2} \cdot P_{H_2}$. This, in turn, was used for calculating the oxygen fugacity from the equilibrium constant (K_w) at pressure and temperature for the reaction $H_2O = H_2 + 0.5\ O_2$ for an experimental assemblage at a given fugacity of H_2O. Thermochemical data for H_2O, H_2, and O_2 and the fugacity of H_2O were taken from Holland and Powell (1998). For many of the experiments where the assemblage is treated under essentially dry conditions, the true f_{O_2} values are most likely lower as the value of f_{O_2} will

decrease with decreasing H_2O activities (Matjuschkin et al., 2015). The water-saturated f_{O_2} equivalent H_2 pressure was set at the Ni-NiO buffer. The accuracy of this method was checked by measuring the f_{O_2} of several runs using metal-metal oxide redox sensors as described in Taylor et al. (1992). The sensor assemblage was H_2O, Co, CoO, and Pd, and was placed into a $Ag_{50}Pd_{50}$ capsule adjacent to the charge. Measured f_{O_2} values were within the margin of error of the calculated f_{O_2} which was ± 0.2 log units.

Analytical methods

Powder X-ray diffraction (XRD) analysis was performed using a Philips Xpert PW3040 diffractometer. Powdered samples were mounted on a zero-background single crystal quartz plate. For unit-cell analysis, small amounts (1-5 wt.%) of synthetic halite were mixed with the sample before scanning to correct the zero-point using the peak positions of halite (a_o = 5.6401Å). The operating conditions were 40 kV and 20 mA using CuKα radiation and fitted with a diffracted-beam graphite monochromator. All samples were scanned from 5-60° 2θ with a step size of 0.04° at 3 seconds per step. The divergent and anti-scatter slits had values of 1.0°. XRD data were analyzed by Rietveld refinements using the General Structure Analysis System (GSAS) software of Larson and Von Dreele (2004).

The crystallographic information files (CIF) used for refinements were: anorthite from Angel (1988), halite from Walker et al. (2004), hastingsite from Makino et al. (1993), hedenbergite from Zhang et al. (1997), magnetite from Wechsler et al. (1984), quartz from Levien et al. (1980), sanidine from Ohashi and Finger (1974), rokühnite ($FeCl_2 \cdot 2H_2O$) from Morosin and Graeber (1965), sylvite from Walker et al. (2004), fayalite from Smyth and Hazen (1977), and annite from Redhammer et al. (2000).

To determine the ferric iron fraction, selected samples were analyzed with Mössbauer

spectroscopy by M. Darby Dyar of Mount Holyoke College. Only about half of the samples were analyzed; the ferric iron fractions of the others were estimated from compositional relationships, as described later. The methods used for Mössbauer spectroscopy in this study were the same as those used for an earlier study of hastingsitic amphiboles (Mueller et al., 2017) which are described in detail in that article. In brief, powdered samples were mixed with sugar under acetone to minimize preferred orientation. Spectra were measured at room temperature for ~24 h using a source of 100–60 mCi ^{57}Co in Rh on a SEE Co. model WT302 spectrometer. Details of the spectrum collection and analysis can be found in Dyar et al. (2006). Error bars for Mössbauer measurements are discussed at length by Dyar (1984) and Dyar et al. (2008). The errors for fits to well-resolved spectra are ± 0.02 mm/s for both the isomer shift (IS) and quadrupolar splitting (QS), and ± 3% absolute for the areas. In many of the spectra studied here, there are multiple overlapping distributions, so the errors are likely slightly higher: ± 0.02–0.05 mm/s for IS and QS with errors of ± 3–5% absolute on areas. Reproducibility (precision) of peak areas based on repeated fits using different constraints (IS, QS, width, and areas constrained in all possible combinations of individual peaks and pairs) and fitting models (Lorentzian, Gaussian, quadrupole splitting distributions) are ±0.3% absolute for well-resolved spectra. Accuracy has been determined in previous studies of amphiboles to be ±3–5% (Dyar, 1989) but is highly dependent on the spectrum being analyzed; a lengthy discussion of this issue is given in Dyar et al. (2008).

Electron microprobe analysis (EMPA) was done at both Binghamton University and Syracuse University. Samples with codes beginning with "HastZ" were analyzed at Binghamton University and those with codes beginning with "ZN" or "KN" were analyzed at Syracuse University. Electron microprobe analysis at Binghamton University was done on a JEOL 8900

Superprobe. The samples were rinsed in deionized water ($^{D}H_2O$) to remove salts that interfere with the epoxy-curing process before mounting in epoxy and being polished with a final diamond grit size of 0.5 µm. Operating conditions were 15 kV and 10 nA. Analyses were done using 10 seconds on peaks and 3 seconds on background for all elements except Cl, which used 30 seconds on peaks and 10 seconds on background. Wollastonite was the standard used for Ca, orthoclase for K, albite for Na, hematite for Fe, quartz for Si, corundum for Al, and reagent grade palladium chloride ($PdCl_2$) for Cl. Matrix corrections were made with the ZAF scheme. Electron microprobe analysis at Syracuse University was done on a Cameca SXFive with a LaB_6 electron gun using powdered samples dispersed over polished graphite rods. The operating conditions were 15 kV and 20 nA using sanidine as the standard for K, jadeite for Na, diopside for Ca and Si, fayalite for Fe, kyanite for Al, and tugtupite for Cl. Analyses were done using 20 second on peaks and 10 seconds on background for all elements except Cl, which used 40 seconds on peaks and 20 seconds on background. Matrix corrections were made with the ZAF scheme.

Analyses were found to be comparable between Syracuse University's microprobe and Binghamton University's microprobe. Mineral formulas were calculated into the general amphibole formula $A_{0\text{-}1}B_2C_5T_8O_{22}W_2$ as discussed in Appendix A. Analysis of fine-grained (2-5 µm wide) minerals often results in the X-ray excitation volume exceeding the volume of the grain and resulting in low analytical totals (Jenkins, 2019). This situation has been studied in considerable detail in this lab (e.g., Giblin et al. 1993; Jenkins and Corona 2006) where it was shown that analyses with analytical totals even as low as 65–70 wt% give stoichiometries that are essentially equivalent to coarser grained minerals. In this study analytical totals below 75 wt. % were discarded. Similarly, samples where B-site total cations ≠ 2.0, C-site total cations ≠ 5, and total cations <15 or >16 were also discarded.

Results

Synthesis products

Amphiboles were synthesized along the hastingsite–potassic-hastingsite join in the presence of $FeCl_2$ brines ranging from 1 to 100 molal. A summary of the run conditions is listed in Table 1, along with the phases produced and the quantity of amphibole (wt. %) present. Figure 2 shows representative back-scattered-electron images of synthetic chloro-hastingsite with coexisting minerals made in Jenkins (2019) at conditions similar to those used here. Amphibole yields were highest when the $FeCl_2$ brine concentration was between 3 and 12 molal. Amphibole yields dropped to ~ 10 wt.% for the most concentrated brine runs of the Na-dominant series (e.g., ZN-50m1 and KN0.25(2)-100m1). Bulk compositions with higher K#'s nucleate amphiboles more readily. The reduction in amphibole yield observed at high brine $FeCl_2$ concentrations can probably be explained by the bulk composition becoming progressively oxygen-reduced with increasing amounts of $FeCl_2$. Supporting this hypothesis, the experiments done at lower brine concentrations always had coexisting magnetite, whereas those done at the highest concentrations contained fayalite instead. Increasing amounts of Fe^{2+} added as $FeCl_2$ reduced the ferric iron fraction of the bulk composition and stabilized the more reduced phase, fayalite. The magnetite-fayalite transition occurred between $FeCl_2$ concentration in the brine of 12 and 24 molal.

During the capsule-weighing procedure after treatment, a fluid would sometimes escape the capsule when punctured, particularly for samples treated at $FeCl_2$ brine concentrations $\leq$ 3m. The color of this fluid was related to the K#. The K-rich samples contained a cloudy white fluid whereas Na-rich samples contained a black fluid. The reason for this is unknown, but might involve a difference in aqueous iron speciation, where K-rich samples have aqueous Fe

277 dominantly in the ferrous state (light color), whereas Na-rich samples have aqueous Fe in mixed
278 valence states causing a strong absorption of light from charge-transfer mechanisms, as seen for
279 minerals (e.g., Nassau, 1978).

280 **Amphibole composition**

281 Only a subset of the samples were analyzed by Mössbauer spectroscopy. Given the
282 higher amphibole yields obtained from K-rich mixtures, the complete series of K# 1.0
283 amphiboles (1 – 100 m $FeCl_2$) were analyzed for their ferric iron fraction (Table 2). The
284 compositions of the samples analyzed by Mössbauer spectroscopy are listed in Table 3a. The
285 O(3) site occupancies for these amphiboles, which were determined by estimation of OH by
286 charge balance and applying the constraint that OH, Cl, and O sum to 2 apfu, are shown in
287 Figure 3. It is noted that attempts to confirm the presence of OH using infrared spectroscopy
288 were unsuccessful because strong absorption from the coexisting minerals (notably magnetite)
289 obscured any OH-stretching signal.

290 Table 3b lists the amphiboles for which Mössbauer analyses were not made. The ferric
291 iron fraction for these samples was estimated in this study using ferric-iron compositional trends
292 observed here for the Mössbauer-analyzed samples. Figure 4a shows the relationship between
293 the initial brine $FeCl_2$ concentration and ferric iron fraction for the amphiboles from Table 3a.
294 There is a positive correlation between the amphiboles' ferric iron fraction and the initial brine
295 $FeCl_2$ concentration from 1 to 24 molal. Between concentrations of 24 and 50 molal, the ferric
296 iron fraction dramatically falls from 0.310 to 0.116. This substantial decrease coincides with a
297 phase change in the mineral assemblage from magnetite to fayalite. This can be explained by a
298 change in the f_{O_2} inside the capsule related to the brine concentration, whereby the system
299 becomes undersaturated with water as the brine becomes more concentrated in $FeCl_2$. In this

300 case, the brine has such a low activity of H_2O that it is no longer able to maintain the desired
301 oxygen buffer near Ni-NiO (Matjuschkin et al., 2015), but instead becomes reduced by the
302 ambient H_2-Ar pressure medium. Dolejš and Wagner (2008) show similar results in their model
303 of the Si-Al-Fe-Mg-Ca-Na-K-H-O-Cl system at elevated *P* and *T*. In their study, the
304 disappearance of biotite (the only Fe-bearing reactant) due to increasing brine salinity led to a
305 sudden decrease in f_{O_2} due to the system losing its oxygen buffer and subsequently having the
306 f_{O_2} controlled by the ambient reducing conditions.

307 Figure 4b shows the relationship between the Cl content of the amphibole and the ferric
308 iron fraction. Amphibole Cl is better correlated with the ferric iron fraction than the initial brine
309 $FeCl_2$ concentration, though both correlations are good, at least up until ~24m (vertical dashed
310 line in Figure 4b). A Deming regression, which accounts for error in both the independent and
311 dependent variables, was used to calculate ferric iron fractions for samples without Mössbauer
312 analysis that were synthesized with brine $FeCl_2$ concentrations < 24m. The equation is:

313 $$Fe^{3+}/Fe^{Total} = 0.0936(wCl) + 0.126 \quad (1)$$

314 The amount of Cl in the amphibole is represented by a normalized wt.% (wCl, 100% analytical
315 total) that excludes any water instead of a recast molar coefficient because recasting the cations
316 required knowledge of the ferric iron fraction, which is what is being solved for. Using a
317 normalized weight percent, though not ideal, provides a relatively unbiased method of removing
318 the variability in the analytical total attending small-grain analyses.

319 The ferric iron concentration of amphiboles synthesized in more concentrated brines was
320 estimated in an alternative method, due to the large change in ferric iron fraction observed
321 between 24 and 50 m $FeCl_2$. Most of the amphiboles synthesized in this study have a sizeable
322 fraction of oxygen on their W or *O(3)* sites (Figure 3). Therefore, the common assumption that

OH + Cl = 2 (e.g., Locock, 2014) is not valid. Recasting of amphibole formulas involves balancing OH and Fe^{3+}/Fe^{Total}, e.g., where increasing Fe^{3+}/Fe^{Total} adds positive charge which must be balanced by substituting OH^- for O^{2-}. Since OH and Fe^{3+}/Fe^{Total} are interdependent, choosing a constant value of OH + Cl can be used to solve for Fe^{3+}/Fe^{Total}. Taking the average and standard deviation of OH + Cl for all the amphiboles with Mössbauer spectra gives a value of 1.465 ± 0.335, which was then used to determine Fe^{3+}/Fe^{Total} by charge balance. This method is simple and only an approximation, but nonetheless was adopted for estimating the ferric iron fraction of amphiboles synthesized with brine $FeCl_2$ molalities > 24m (Table 3b).

Analysis of the data indicates some trends which are shown in Figures 5 through 7. Figure 5 shows the relationship between total *A*-site cations (Σ*A*) and amphibole Cl (apfu). The trend is negative at first, with Σ*A* decreasing with increasing Cl, reaching a minimum at Cl ~ 0.45 apfu, and turning positive above it. The inflection point of this V-shaped trendline coincides with the magnetite-fayalite transition and the drop in the ferric iron fraction (Figures 4a,b). This suggests a connection between Σ*A* and Fe^{3+}/Fe^{Total}. Figure 6 shows how both Σ*A* and $^{C}Fe^{3+}$ vary with respect to amphibole Cl and it is apparent that any increase in $^{C}Fe^{3+}$ corresponds to a quasi-proportionate decrease in Σ*A*. This can be represented by the following exchange reaction: $A^+ + Fe^{2+} \rightleftharpoons \square + Fe^{3+}$, where □ is an *A*-site vacancy, and is supported by the generally negative correlation between Σ*A* and $^{C}Fe^{3+}$ shown in Figure 7.

Brine-amphibole interactions

Initial brine $FeCl_2$ concentrations were calculated using the total amount of $FeCl_2$ added to the capsule, the amount of water added to the capsule, and the amount of water contained within the structure of $FeCl_2 \cdot nH_2O$ as determined via XRD. This represents the brine concentration at the beginning of treatment at elevated *P* and *T*, assuming the brine is below

346 saturation in $FeCl_2$. These are reported as initial brine concentrations because it is possible for
347 the brine to have evolved during treatment by reaction with the solids. Figure 8 shows the
348 relationship between the mole fraction of Cl in the brine and amphibole Cl content for
349 amphiboles of varying K#. The relationship is a linear, positive trend, with amphibole Cl
350 increasing as the brine becomes more Cl-rich. Furthermore, all the amphiboles of varying K# lie
351 along an identical $^{amph}O(3)_{Cl}$ - $^{brine}X_{Cl}$ slope, indicating that for Mg-free amphiboles, K# does not
352 influence Cl incorporation.

353 A crude estimate of the Cl concentration of the brine at the end of treatment can be
354 calculated using the weight change of each capsule after being punctured and heated to 110 °C as
355 discussed above. This method assumes that all mass lost when heating the punctured capsule is
356 due to water evaporation. This method, as mentioned previously, probably gives a minimum
357 estimate in the total water content available because of structurally bound water in any solid
358 $FeCl_2$ that precipitated after the experiment, which means that calculated brine Cl concentrations
359 are over estimated. Annite, which was only observed in two experiments and is present at a small
360 (< 5 wt%) amounts, has little effect on the water assessment. It is anticipated that dilute $FeCl_2$
361 brines will have smaller amounts of $FeCl_2 \cdot nH_2O$ whereas more concentrated brines have larger
362 amounts and thereby contain more water bound in $FeCl_2 \cdot nH_2O$. A comparison of the initial and
363 final brine Cl concentrations is shown in Figure 9. This figure suggests that the low-
364 concentration brines did not evolve much during treatment, because their initial brine
365 concentrations are nearly identical to their final (post-treatment) concentrations. At high brine
366 concentrations, however, the final concentrations are overestimated and thus do not allow the
367 evolution of the brine to be determined.

368 **Discussion**

The role of ferric iron

The positive correlation between the ferric iron fraction and amphibole Cl content observed at low Cl values as shown in Figure 4b is noteworthy both because it reverses after the appearance of fayalite, where a sudden reductive jump occurs at brine $FeCl_2$ concentrations between 24 and 50 molal, and because it contradicts earlier work. The positive correlation implies that amphibole Fe^{3+} plays a positive role in Cl incorporation. In contrast, the study of Mueller et al. (2017), which synthesized a series of amphiboles along the hastingsite - magnesio-hastingsite join, observed a negative correlation between Fe^{3+} and Cl, with the most Mg-rich samples having the highest proportion of Fe^{3+}. Though their amphiboles were synthesized without the addition of water (i.e., "dry"), the high pH_2 pressure (200 psi) used to control the fO_2 near Co-CoO could have allowed for substantial absorption of H_2 into the capsule. This, in turn, could react with any oxygen (free O_2 or in reagent Fe_2O_3) in the capsule to form water and an evolved brine during treatment. This study did observe that more reducing fO_2 values were correlated with larger amounts of mass gained by the capsule during treatment, which would be expected if increasing amounts of H_2 were being absorbed. Unfortunately, there is insufficient data to adequately test this hypothesis. In view of the present results, the correlations between Fe^{3+} and Cl in Mueller et al. (2017) and in this study may be related to the crystal-chemistry of Mg-rich hastingsites or have been caused by changes in brine chlorinity, respectively.

Potassium, sodium, and chlorine

Naturally occurring chloro-amphiboles display certain chemical trends, implying crystal chemical constraints on Cl incorporation into amphiboles. Roughly half of the studies on chloro-amphiboles show a positive correlation between K and Cl, and Na and Cl, including Vanko (1986), Enami et al. (1992), Sautter et al. (2006), Kendrick et al. (2015), and Yu et al. (2017)

(Figure 10). The other half show a positive correlation between K and Cl, but a negative correlation between Na and Cl, including Castelli (1988), Léger et al. (1996), Kullerud (1996), Henry and Daigle (2018), and Gilland et al. (2021) (Figure 11). There are also a handful of studies with unclear data, and report varying correlations between the *A*-cations and Cl (Lui et al., 2009). Overall, previous work on chloro-amphiboles indicates: (1) Σ*A*-site cations are positively correlated with the amphibole Cl content, and (2) there are conflicting signals as to whether the occupant of the *A*-site (K vs Na) has an influence on amphibole Cl.

This study clearly indicates that both K-rich and Na-rich amphiboles behave similarly. Not only do they incorporate Cl comparably, but they also respond similarly to changes in ferric iron fraction by adding or removing *A*-site cations to maintain charge balance ($A^{+} + Fe^{2+} \leftrightharpoons \square + Fe^{3+}$). The only observed difference between K- and Na-rich amphiboles in this study was that amphibole yield increased as amphibole K# increased. These findings suggest that the K# of Cl-bearing hastingsite is controlled by the activity ratio aK/aNa of the brine, or more broadly the amphibole-forming fluid environment. It should also be noted that the K# for the amphiboles in this study mirrored the K# of the starting bulk compositions (the partitioning of K/Na between the amphibole and the brine ~ 1).

What is still unclear is whether *A*-site occupancy constrains amphibole Cl incorporation. The literature suggests that it does, but the literature also suggests that K enhances amphibole Cl uptake for amphiboles that generally contain at least some Mg. The V-shaped correlation between Σ*A* and Cl shown in Figure 5 might be interpreted in a manner that indicates Σ*A* does not affect Cl incorporation, due to both a positive *and* a negative correlation. In this study, where the amphibole is devoid of Mg, this change in correlation is most likely controlled by the ferric iron content of the amphibole. Preliminary attempts in this study to synthesize chloro-

This is the peer-reviewed, final accepted version for American Mineralogist, published by the Mineralogical Society of America.
The published version is subject to change. Cite as Authors (Year) Title. American Mineralogist, in press.
DOI: https://doi.org/10.2138/am-2023-9083. http://www.minsocam.org/

amphiboles without *A* cations, such as chloro-ferro-hornblende ($Ca_2(Fe^{2+}_4Al)(AlSi_7)O_{22}Cl_2$) and chloro-ferro-actinolite ($Ca_2Fe^{2+}_5Si_8O_{22}Cl_2$), were not successful, suggesting the presence of an *A*-cation is important to stabilize Cl-bearing amphiboles. At present the exact nature of this dynamic is unclear, that is whether it is dominated by crystal structure issues, including the need for a minimum *A*-cation content to allow significant Cl incorporation, or the chemical bonding between the *A*-site cation and the O(3) anion.

Implications

The observation in this study that Na and K essentially have the same effect on Cl incorporation into hastingsitic amphiboles (Fig. 8) stands in contrast to the earlier study of Jenkins (2019) where K was found to be more effective than Na. As noted by Jenkins (2019), the brine concentrations were not all identical for these experiments; however, the implication from this study is that the ferric-iron proportion may actually have been the controlling factor, rather than the K#.

Probably the main geological application for this research is to determine the Cl concentration of the brine from which Cl-rich amphiboles form. The present study provides important information on Mg-free hastingsitic amphiboles and thereby addresses one end-member of the spectrum of Cl-bearing calcium amphiboles observed in nature (e.g., Giesting and Filiberto, 2016). Although it is tempting to use Figure 8 for this purpose, it must be stressed that this study does not account for the Mg-Cl avoidance mentioned earlier and which must be considered if we are to extract meaningful Cl concentrations from a given mineral assemblage. Such a treatment, based on the data in Matteucci (2022), will be presented in a separate manuscript.

This study may also shed some light on why most (terrestrial) calcium amphiboles do not

438 achieve the predicted maximum of 2.0 Cl apfu (e.g., Giesting and Filiberto, 2016). A simple
439 straight-line extrapolation of the bine concentration vs Cl content of Figure 8 indicates a
440 maximum Cl content of only about 1.2 apfu in the presence of pure $FeCl_2$. Unfortunately, direct
441 experimental verification that the line remains linear up to pure $FeCl_2$ is not possible with the
442 methods used in this study because of the hygroscopic nature of $FeCl_2$. Even if $FeCl_2$ was able
443 to be added to the capsule in a completely anhydrous state, hydrogen diffusion through the
444 permeable $Ag_{50}Pd_{50}$ capsule from the pressure medium during treatment at elevated *P*-*T*
445 conditions would undoubtedly form some water by such reactions as $3Fe_2O_3 + H_2 \rightarrow 2Fe_3O_4 +$
446 H_2O. This is supported by experiments whenever a chloro-amphibole is synthesized "dry",
447 whereby the capsule absorbs mass during the treatment attributed to the formation of water. The
448 water in these experiments after treatment has been confirmed through mass lost on heating to
449 110 °C. Until such thoroughly anhydrous experiments can be done, it is unclear from this study
450 that amphiboles with Cl contents above 1.2 apfu could be formed from a brine. Reports of
451 calcium amphiboles with up to 2.0 Cl apfu have so far only been found as very small daughter
452 crystals occurring in melt inclusions in host minerals in Martian meteorites, most notably the
453 nakhlite MIL 03346 (Sautter et al., 2006; McCubbin et al. 2009; Giesting and Filiberto, 2016;
454 Martínez et al., 2023). Results from this study would suggest that end-member chloro-
455 amphibole requires the presence of a coexisting melt that accepts water more readily than the
456 amphibole. Experimental evidence for the preferential incorporation of Cl over H_2O into
457 magmatic amphibole is still in need of confirmation but has been suggested for magmas
458 undersaturated in H_2O by the study of Cannaò et al. (2022).
459 Although the findings of this study involving Mg-free amphiboles suggest that K-rich and
460 Na-rich amphiboles incorporate Cl similarly, the fact that K and Cl are positively correlated in

461 virtually every natural amphibole reported in the literature must be explained. The origin of this
462 correlation is not known at present but may arise from some process where K is the dominant
463 cation in the amphibole-forming brine or that K is preferentially partitioned into calcium
464 amphibole. The former case is certainly possible though not so likely given the preponderance of
465 Na over K in most natural waters (e.g., Drever, 1997) and a lack of fluid-inclusion analyses to
466 test this hypothesis. One example of the latter case is the alkali-chloride metasomatism observed
467 for mafic rock bulk compositions where K partitions preferentially into calcium amphibole while
468 Na partitions into plagioclase and scapolite (Johnson et al., 2004). Such partitioning was not
469 observed here but could potentially occur with the appropriate coexisting mineral assemblage.
470 Further review of the literature indicates that there is no preference for K-rich or Na-rich
471 chloro-amphiboles based on geologic setting. Of the studies listed earlier, there is one attribute
472 that separates the chloro-amphiboles that have a positive correlation between Na and Cl from
473 those that have a negative correlation: age. The rocks that contain Cl-rich amphiboles with a
474 positive correlation between both *A*-cations and Cl are younger, formed in the Phanerozoic (e.g.,
475 Mathematician Ridge, Vanko, 1985; Dabie-Sulu orogenic belt, Xiao et al., 2005; Qiman Tagh
476 metallogenic belt, Yu et al., 2017), whereas those with a negative correlation between Na and Cl
477 are older (Archean and Proterozoic) (e.g., Hudson Highlands, Léger et al., 1996 and Gilland et
478 al., 2021; Flakstadøy Basic Complex, Kullerud, 1996; Beartooth Mtns, Henry and Daigle, 2018).
479 Whether there is some process that enriches chloro-amphiboles in K as they age is not known,
480 nor is it known if this relationship exists in chloro-amphiboles from other regions. This
481 hypothesis, if verified with additional data, may point to a gradual change in the geochemical
482 controls on chloro-amphibole formation that is similar in nature to the preferential formation of
483 dolomite over calcite in the ancient geological record (e.g., Fang and Xu, 2022).

Funding

Financial support for this study comes from National Science Foundation grant EAR-1725053.

Acknowledgements

We are very grateful to David Collins and Jay Thomas for their help with the microprobe analyses at Binghamton University and Syracuse University, respectively. The manuscript was greatly improved by the reviews of Darrell Henry, David Dolejš, and an anonymous reviewer. Use of the program VESTA, version 3.90.0a, by K. Momma and F. Izumi for producing the structure in Supplemental Figure 1 is gratefully acknowledged.

References Cited

Angel, R.J. (1988). High-pressure structure of anorthite. American Mineralogist, 73, 1114-1119.

Aranovitch, L.Y, and Newton, R.C. (1997). H2O activity in concentrated KCl and KCl-NaCl solutions at high temperatures and pressures measured by the brucite-periclase equilibria. Contributions to Mineralogy and Petrology, 127, 261-271.

Campanaro, B.P., and Jenkins, D.M. (2017). An experimental study of chlorine incorporation in amphibole synthesized along the pargasite--ferro-pargasite join. Canadian Mineralogist, 55, 419-436.

Cannaò, E., Schiavi, F., Casiraghi, G., Tiepolo, M., and Fumagalli, P. (2022) Effect of chlorine on water incorporation in magmatic amphibole: experimental constraints with a micro-Raman spectroscopy approach. European Journal of Mineralogy, 34, 19-34.

Castelli, D. (1988). Chlorpotassium ferro-pargasite from Sesia-Lanzo marbles (Western Italian Alps): a record of highly saline fluids. Società Italiana di Mineralogia e Petrologia, 43, 129-138.

Chan, A., Jenkins, D.M., and Dyar, M.D. (2016). Partitioning of chlorine between NaCl brines and ferro-pargasite: implications for the formation of chlorine-rich amphiboles in mafic rocks. Canadian Mineralogist, 54, 337-351.

Chu, L., Enggist, A., and Luth, R.W. (2011). Effect of KCl on melting in the Mg_2SiO_4-$MgSiO_3$-H_2O system at 5 GPa. Contributions to Mineralogy and Petrology, 162, 565-571.

Dolejš, D., and Wagner, T. (2008). Thermodynamic modeling of non-ideal mineral–fluid equilibria in the system Si–Al–Fe–Mg–Ca–Na–K–H–O–Cl at elevated temperatures and pressures: Implications for hydrothermal mass transfer in granitic rocks. Geochimica et Cosmochimica Acta, 72, 526-553.

Drever, J.I., (1997). The Geochemistry of Natural Waters: Surface and Groundwater Environments. Prentice-Hall, Inc., Upper Saddle River, NJ, 436 pp.

Driesner, T., and Heinrich, C.A. (2007). The system H_2O-NaCl. Part I: Correlation formulae for phase relations in temperature-pressure-composition space from 0 to 1000 °C, 0 to 5000 bar, and 0 to 1 XNaCl. Geochimica et Cosmochimica Acta, 71, 4880-4901.

Dyar, M.D. (1984). Precision and interlaboratory reproducibility of measurements of the Mössbauer effect in minerals. American Mineralogist, 69, 1127–1144.

Dyar, M.D. (1989). Application of Mössbauer goodness-of-fit parameters to experimental spectra: further discussion. American Mineralogist, 74, 688.

Dyar, M.D., Agresti, D.G., Schaefer, M., Grant, C.A., and Sklute, E.C. (2006). Mössbauer

spectroscopy of earth and planetary materials. Annual Review of Earth and Planetary Sciences, 34, 83–125.

Dyar, M.D., Schaeffer, M.W., Sklute, E.C., and Bishop, J.L. (2008). Mössbauer spectroscopy of phyllosilicates: effects of fitting models on recoil-free fractions and redox ratios. Clay Minerals, 43, 3–33.

Enami, M., Liou, J.G., Bird, D.K. (1992). Cl-bearing amphibole in the Salton Sea geothermal system, California. Canadian Mineralogist, 30, 1077-1092.

Fang, Y., and Xu, H. (2022) Dissolved silica-catalyzed disordered dolomite precipitation. American Mineralogist, 107, 443-452.

Frezzotti, M.L., and Ferrando, S. (2015). The chemical behavior of fluids released during deep subduction based on fluid inclusions. American Mineralogist, 100, 352-377

Frost, B.R. (1991). Introduction to oxygen fugacity and its petrologic importance. In, D. H. Lindsley, ed., Oxide minerals: petrologic and magnetic significance. Reviews in Mineralogy, 25, 1-9.

Giblin, L.E., Blackburn, W.H., and Jenkins, D.M. (1993) X-ray continuum discrimination technique for the energy dispersive analysis of fine particles. Analytical Chemistry, 65, 3576–3580.

Giesting, P.A., and Filiberto, J. (2016). The formation environment of potassic-chloro-hastingsite in the nakhlites MIL 03346 and pairs and NWA 5790: Insights from terrestrial chloro-amphibole. Meteoritics and Planetary Science, 51, 2127-2153.

Gilland, A.J., Hebert, L.I., Javier-Jimenez, D.R., Masi, J.K., Meyler, S.R., Schwartz, S.G., Verhaeg, E.A., Hughes, J.M., Lincoln, E.S., O'Brien G.P., Powers, S.K., Schireman R.G., Lupulescu, M.V., and Bailey, D.G. (2021). Chlorine-rich amphiboles from the Grenville-age Hudson Highlands of New York state. Canadian Mineralogist, 59, 139-148.

Henry, D.J., and Daigle, N.M. (2018). Chlorine incorporation into amphibole and biotite in high-grade iron-formations: Interplay between crystallography and metamorphic fluids. American Mineralogist, 103, 55-68.

Holland, T.J.B., and Powell, R. (1998) An internally consistent thermodynamic data set for phases of petrological interest. Journal of Metamorphic Geology, 16, 309-343.

Jenkins, D.M. (2019). The incorporation of Cl into calcium amphiboles. American Mineralogist, 104, 514-524.

Jenkins, D.M., and Corona, J.C. (2006) The role of water in the synthesis of glaucophane. American Mineralogist, 91, 1055–1068.

Johnson, E.L, Goergen, E.T., and Fruchey, B.L. (2004). Right lateral oblique slip movements followed by post-Ottawan (1050-1020 Ma) orogenic collapse along the Carthage-Colton shear zone: Data from the Dana Hill metagabbro body, Adirondack Mountains, New York, in Tollo, R.P., Corriveau, L., McLelland, J., and Bartholomew, M.J., eds, Proterozoic tectonic evolution of the Grenville orogen in North America: Boulder, Colorado, Geological Society of America Memoir 197, p. 357-378.

Kendrick, M.A., Honda, M., and Vanko, D.A. (2015). Halogens and noble gases in Mathematician Ridge meta-gabbros NE Pacific: implications for oceanic hydrothermal root zones and global volatile cycles. Contributions to Mineralogy and Petrology, 170:43.

Kullerud, K. (1996). Chlorine-rich amphiboles: interplay between amphibole composition and an evolving fluid. European Journal of Mineralogy, 8, 355-370.

Kusebauch, C., John, T., Barnes, J.D., Klügel, A., and Austrheim, H.O. (2015). Halogen element and stable chlorine isotope fractionation caused by fluid-rock interaction (Bamble Sector, SE Norway). Journal of Petrology, 56, 299-324.

Legér, A., Rebbert, C., and Webster, J. (1996). Cl-rich biotite and amphibole from Black Rock Forest, Cornwall, New York. American Mineralogist, 81, 495-504.

Levien , L., Prewitt, C.T., and Weidner, D.J. (1980). Structure and elastic properties of quartz at pressure. American Mineralogist, 65, 920-930.

Locock, A.J. (2014). An Excel spreadsheet to classify chemical analyses of amphiboles following the IMA 2012 recommendations. Computers and Geosciences, 62, 1-11.

Lui, J., Lui, W., Ye, K., and Mao, Q. (2009). Chlorine-rich amphibole in Yangkou eclogite, Sulu ultrahigh-pressure metamorphic terrane, China. European Journal of Mineralogy, 21, 1265-1285.

Makino, K., Tomita, K., and Suwa, K. (1993). Effect of chlorine on the crystal structure of a chlorine-rich hastingsite. Mineralogical Magazine, 57, 677-685.

Martínez, M., Shearer, C.K., and Brearley, A.J. (2023). Ferro-chloro-winchite in Northwest Africa (NWA) 998 apatite-hosted melt inclusion: New insights into the nakhlite parent melt. Geochimica et Cosmochimica Acta, 344, 122-133.

Matjuschkin, V., Brooker, R.A., Tattich, B., Blundy, J.D., and Stamper, C.C. (2015). Control and monitoring of oxygen fugacity in piston cylinder experiments. Contributions to Mineralogy and Petrology, 169, 9.

Matteucci, J. P. (2022) Experimental studies of the crystal structure, pressure-temperature stability, and chlorine partitioning of hastingsitic amphiboles, 156 p. Ph.D. thesis, Binghamton University.

McCubbin, F.M., Tosca, N.J., Smirnov, A., Nekvasil, H., Steele, A., Fries, M., and Lindsley, D.H. (2009) Hydrothermal jarosite and hematite in a pyroxene-hosted melt inclusion in Martian meteorite Miller Range (MIL) 03346: Implications for magmatic-hydrothermal fluids on Mars. Geochimica et Cosmochimica Acta 73, 4907-4917.

Morosin B., and Graeber E.J. (1965). Crystal structures of manganese (II) and iron (II) chloride dihydrate. Journal of Chemical Physics, 42, 898-901.

Morrison, J. (1991). Compositional constraints on the incorporation of Cl-into amphiboles. American Mineralogist, 76, 1920-1930.

Mueller, B.L., Jenkins, D.M., and Dyar, D.M. (2017). Chlorine acceptance in amphiboles synthesized along the magnesio-hastingsite--hastingsite compositional join. European Journal of Mineralogy, 29, 167-180.

Munoz, J.L. (1984). F-OH and Cl-OH exchange in micas with application to hydrothermal ore deposits. In, S. W. Bailey (ed.) Micas. Reviews in Mineralogy, 13, 469-493.

Nassau, K. (1978). The origins of color in minerals. American Mineralogist, 63, 219-229.

Newton, R.C., and Manning, C.E. (2010). Role of saline fluids in deep-crustal and upper-mantle metasomatism: insights from experimental studies. Geofluids, 10, 58-72.

Ohashi, Y., and Finger, L.W. (1974). Refinement of the crystal structure of sanidine at 25 and 400C. Carnegie Institution of Washington: Yearbook 73, 539-544.

Redhammer, G.J., Beran, A., Schneider, J., Amthauer, B., and Lottermoser, W. (2000). Spectroscopic and structural properties of synthetic micas on the annite-siderophyllite binary: Synthesis, crystal structure refinement, Mössbauer, and infrared spectroscopy. American Mineralogist, 85, 449-465.

Sautter, V., Jambon, A., and Boudouma, O. (2006). Cl-amphibole in the nakhlite MIL 03346: Evidence for sediment contamination in a Martian meteorite. Earth and Planetary Science Letters, 252, 45-55.

Selverstone, J., and Sharp, Z.D. (2011) Chlorine isotope evidence for multicomponent mantle metasomatism in the Ivrea Zone. Earth and Planetary Science Letters, 310, 429-440.

Shaw, H.R., and Wones, D.R. (1964). Fugacity coefficients for hydrogen gas between O degrees and 1000 degrees C, for pressures to 3000 atm. American Journal of Science, 262 (7), 918-929.

Smyth, J.R., and Hazen, R.M. (1973). The crystal structure of forsterite and hortonolite at several temperatures. American Mineralogist, 58, 588-593.

Taylor, J.R, Wall, V.J., and Pownceby, M.I. (1992). The calibration and application of accurate

679 redox sensors. American Mineralogist, 77, 284-295.
680
681 Vanko, D.A. (1986). High chlorine amphiboles from oceanic rocks: product of highly saline
682 hydrothermal fluids? American Mineralogist, 71, 51-59.
683
684 Walker, D., Cranswick, L.D., Jones, R.L., Clark, S.M., and Buhre, S. (2004). Halite-sylvite
685 thermoelasticity. American Mineralogist, 89, 204-210.
686
687 Weast, R.C. ed. (1978). CRC Handbook of Chemistry and Physics, 58th ed., CRC Press, Inc.,
688 West Palm Beach, Florida, USA.
689
690 Wechsler, B.A., Lindsley, D.H., and Prewitt, C.T. (1984). Crystal structure and carbon
691 distribution in titanomagnetites. American Mineralogist, 69, 754-770.
692
693 Weidner, J.R. (1989). Welding silver and silver alloy containers for high-temperature and high-
694 pressure experiments. American Mineralogist, 74, 1385.
695
696 Xiao, Y., Hoefs, J., and Andreas, K. (2005). Compositionally zoned Cl-rich amphiboles from
697 North Dabie Shan, China: Monitor of high-pressure metamorphic fluid/rock interaction
698 processes. Lithos, 81, 279-295.
699
700 Yardley, B.W.D., and Graham, J.T. (2002). The origins of salinity in metamorphic fluids.
701 Geofluids, 2, 249-256.
702
703 Yardley, B., and Bodnar, R.I. (2014). Fluids in the Continental Crust. Geochemical Perspectives
704
705 Yu, M., Feng, C.Y., Zhu, Y.F., Mao, J.W., Zhao, Y.M., and Li, D.X. (2017). Multistage
706 amphiboles from the Galinge skarn deposit in Qiman Tagh, western China: evidence of
707 igneous rocks replacement. Mineralogy and Petrology, 111, 81-97.
708
709 Zhang, L., Ahsbahs, H., Hafner, S.S., and Kutoglu, A. (1997). Single-crystal compression and
710 crystal structure of clinopyroxene up to 10 GPa. American Mineralogist, 82, 245-258.
711
712

713
714 **Table 1.** Summary of run conditions and products.

Sample Code	K#	T (°C)	P (kbar)	t (hrs)	Δf_{O_2} *	Products	Wt.% Amph
ZN-1m1	0	699 (8)	3.05 (5)	96	0.01	Amph, Cpx, Ab, Mt, Ht	39.5 (6)
ZN-3m1	0	703 (4)	3.08 (5)	96	0.05	Amph, Cpx, Ab, Mt, Ht	64.8 (8)
ZN-12m1	0	699 (10)	3.08 (5	96	0.00	Amph, Cpx, Ab, Fay, Mt, Ht	56.6 (8)
ZN-50m1	0	702 (6)	3.15 (5)	96	0.00	Amph, Cpx, Ab, Fay, Ht	10.3 (7)
KN0.25(2)-1m1	0.25	699 (8)	3.05 (5)	96	0.01	Amph, Cpx, Plag, Mt, Sylv, Ann, HS_{ss}	58.3 (8)
KN0.25(2)-3m1	0.25	695 (13)	3.00 (5)	96	0.00	Amph, Cpx, Plag, Mt, HS_{ss}	75.4 (8)
KN0.25(2)-12m1	0.25	701 (8)	3.06 (5)	132	0.01	Amph, Cpx, Plag, Fay, Mt, Qtz, HS_{ss}	65.4 (9)
KN0.25(2)-50m1	0.25	698 (8)	3.02 (5)	96	0.01	Amph, Cpx, Plag, Fay, HS_{ss}	51.6 (9)
KN0.25(2)-100m1	0.25	697 (10)	3.02 (5)	96	0.01	Amph, Cpx, Plag, Fay, Qtz, HS_{ss}, Rkn	12.2 (15)
KN0.50-1m1	0.5	699 (8)	2.98 (5)	96	0.02	Amph, Cpx, Plag, Mt, Qtz, HS_{ss}	77.1 (8)
KN0.50-3m1	0.5	697 (11)	3.00 (5)	96	0.01	Amph, Cpx, Plag, Mt, HS_{ss}	78.7 (7)
KN0.50-12m1	0.5	697 (7)	3.10 (5)	96	-0.01	Amph, Cpx, Plag, Fay, Mt, HS_{ss}, Rkn	69.7 (8)
KN0.50-50m1	0.5	694 (14)	3.00 (5)	96	0.00	Amph, Cpx, Plag, Fay, Qtz, HS_{ss}	53.4 (8)
KN0.50-100m1	0.5	695 (11)	3.10 (5)	96	-0.02	Amph, Cpx, Plag, Fay, Qtz, HS_{ss}	43.0 (9)

715
716

Table 1. Continued

Sample Code	K#	T (°C)	P (kbar)	t (hrs)	f_{O_2} *	Products	Wt.% Amph
KN0.75-1m1	0.75	691 (19)	3.00 (5)	96	-0.01	Amph, Cpx, Plag, Mt, HS_{ss}, Ann	52.7 (7)
KN0.75-3m1	0.75	701 (7)	3.10 (5)	96	0.01	Amph, Cpx, Mt, HS_{ss}	84.6 (21)
KN0.75-12m1	0.75	697 (11)	3.08 (5)	96	-0.01	Amph, Cpx, Plag, Mt, Qtz, HS_{ss}	84.9 (9)
KN0.75-50m1	0.75	701 (7)	3.01 (5)	96	0.02	Amph, Cpx, Plag, Fay, Rkn	47.7 (8)
KN0.75-100m1	0.75	695 (10)	3.08 (5)	96	-0.01	Amph, Cpx, Plag, Fay, Rkn	39.5 (9)
HastZ-1m2	1	701 (5)	3.00 (5)	96	0.02	Amph, Cpx, An, Mt, Sylv	76.2 (11)
HastZ-2m2	1	701 (8)	3.05 (5)	96	0.02	Amph, Cpx, An, Mt, Sylv	83.3 (10)
HastZ-3m1	1	700 (4)	3.00 (5)	96	0.02	Amph, Cpx, An, Mt, Sylv	84.2 (7)
HastZ-6m1	1	700 (6)	3.04 (5)	96	0.01	Amph, An, Mt, Sylv	89.0 (11)
HastZ-12m1	1	700 (2)	3.02 (5)	96	0.00	Amph, Cpx, An, Mt, Qtz, Sylv, Rkn	80.9 (9)
HastZ-24m2	1	701 (2)	3.08 (5)	96	0.00	Amph, Cpx, An, Mt, Qtz, Rkn	71.9 (10)
HastZ-50m1	1	700 (2)	2.98 (5)	96	0.02	Amph, Cpx, An, Fay, Qtz	78.0 (8)
HastZ-100m1	1	687 (2)	3.05 (5)	96	-0.03	Amph, Cpx, An, Fay, Qtz	78.9 (7)

* Log oxygen fugacity relative to the Ni-NiO oxygen buffer of Frost (1991)

Note: Uncertainties (1σ) in the last digit are given in parentheses. K# is the molar ratio = $\frac{K}{Na+K}$. Brine $FeCl_2$ molalities are in the sample code (e.g., sample ZN-3m1 has a brine molality of 3). f_{O_2} was calculated using the P, T, and X_{H_2} of the pressure media. Abbreviations: Ab = albite, An = anorthite, Ann = annite, Amph = amphibole, Cpx = hedenbergitic clinopyroxene, Fay = fayalite, Ht = halite, HS_{ss} = halite-sylvite solid solution, Mt = magnetite, Plag = plagioclase, Qtz = quartz, Rkn = rokuhnite, Sylv = sylvite.

This is the peer-reviewed, final accepted version for American Mineralogist, published by the Mineralogical Society of America.
The published version is subject to change. Cite as Authors (Year) Title. American Mineralogist, in press.
DOI: https://doi.org/10.2138/am-2023-9083. http://www.minsocam.org/

728
729
730 **Table 2.** Mössbauer spectra fitting parameters, crystallographic site occupancies, and bulk ferric
731 iron contents.
732

Iron type and site occupancy	Parameter	Sample Code							
		HasZ -1m2	HasZ -2m2	HasZ -3m1	HasZ -6m1	HastZ -12m1	HasZ-24m2	HasZ-50m1	HasZ-100m1
Oct Fe^{3+}	IS	0.51	0.50	0.48	0.46	0.44	0.43	0.49	0.50
	QS	0.59	0.61	0.55	0.54	0.59	0.59	0.58	0.57
	Width	0.48	0.48	0.40	0.39	0.41	0.38	0.38	0.46
	Area	16	17	16	18	22	28	12	13
Oct Fe^{2+} M(4)	IS	1.10	1.12	1.08	1.05	1.06	1.07	1.09	1.10
	QS	2.06	2.14	2.09	2.00	2.08	2.13	2.21	2.23
	Width	0.43	0.42	0.38	0.31	0.34	0.29	0.34	0.43
	Area	18	24	17	13	15	15	28	31
Oct Fe^{2+} M(2)	IS	1.14	1.14	1.14	1.11	1.11	1.12	1.12	1.12
	QS	2.49	2.06	2.47	2.39	2.44	2.47	2.61	2.63
	Width	0.38	0.28	0.30	0.27	0.25	0.23	0.25	0.28
	Area	40	22	27	22	17	20	28	30
Oct Fe^{2+} M(1) M(3)	IS	1.15	1.15	1.14	1.13	1.13	1.13	1.15	1.16
	QS	2.81	2.81	2.81	2.73	2.74	2.76	2.85	2.88
	Width	0.26	0.26	0.26	0.26	0.26	0.26	0.26	0.26
	Area	15	21	21	30	22	27	33	26
$\%Fe^{3+}$		17.6	20.4	20.4	21.9	28.9	31.0	11.6	12.8

733
734 Abbreviations: IS = isomer shift (mm/s); QS = quadrupole splitting (mm/s). Width is the full
735 width at half maximum (mm/s), while the Area is given as the percentage of the total peak area
736 in each doublet.
737

738 **Table 3a.** Compositions of amphiboles synthesized at the conditions listed in Table 1 for which
739 ferric iron content was measured.
740

Exp Name	HasZ-1m2	HasZ-2m2	HasZ-3m1	HasZ-6m1
n	16	18	17	19
SiO_2	38.13 (94)	37.82 (135)	36.69 (189)	38.53 (207)
Al_2O_3	10.32 (103)	9.67 (46)	10.54 (99)	9.99 (85)
FeO	26.69 (86)	25.75 (84)	25.14 (98)	24.75 (117)
Fe_2O_3	6.32 (61)	7.33 (70)	7.23 (72)	7.71 (79)
CaO	10.60 (33)	10.32 (44)	10.63 (48)	10.00 (38)
Na_2O	0	0	0	0
K_2O	3.42 (13)	3.14 (14)	2.73 (13)	2.32 (24)
Cl	0.54 (6)	0.62 (7)	0.83 (9)	1.01 (14)
H_2O*	1.19 (17)	1.06 (12)	1.21 (13)	0.85 (13)
Total	95.38 (147)	93.92 (215)	93.06 (375)	93.54 (412)
Site assignments				
^{T}Si	6.45 (15)	6.50 (9)	6.33 (8)	6.60 (10)
^{T}Al	1.55 (15)	1.50 (9)	1.67 (8)	1.40 (10)
$^{T}Fe^{3+}$	0.00 (0)	0.00 (0)	0.00 (0)	0.00 (0)
Sum T	8	8	8	8
^{C}Al	0.51 (8)	0.46 (7)	0.47 (16)	0.62 (12)
$^{C}Fe^{3+}$	0.80 (2)	0.95 (2)	0.93 (5)	1.00 (2)
$^{C}Fe^{2+}$	3.69 (7)	3.59 (6)	3.60 (12)	3.39 (10)
Sum C	5	5	5	5
^{B}Fe	0.08 (5)	0.11 (4)	0.04 (3)	0.17 (3)
^{B}Ca	1.92 (5)	1.89 (4)	1.96 (3)	1.83 (3)
Sum-B	2	2	2	2
^{A}Na	0	0	0	0
^{A}K	0.74 (3)	0.69 (4)	0.60 (3)	0.51 (5)
^{A}Ca	0.00 (0)	0.01 (1)	0.01 (1)	0.00 (0)
Sum-A	0.74 (3)	0.70 (4)	0.61 (3)	0.51 (5)
Cations	15.74 (3)	15.69 (4)	15.61 (3)	15.51 (5)
Cl	0.15 (2)	0.18 (2)	0.24 (3)	0.29 (4)
OH	1.34 (16)	1.22 (10)	1.41 (15)	0.97 (14)
Anions	1.49 (15)	1.40 (10)	1.65 (16)	1.27 (14)
Fe^{3+}/Fe^{total}	0.176 (9)	0.204 (10)	0.204 (10)	0.219 (11)

741
742
743
744
745
746

This is the peer-reviewed, final accepted version for American Mineralogist, published by the Mineralogical Society of America.
The published version is subject to change. Cite as Authors (Year) Title. American Mineralogist, in press.
DOI: https://doi.org/10.2138/am-2023-9083. http://www.minsocam.org/

Table 3a. (continued)

Exp Name	HastZ-12m1	HasZ-24m2	HasZ-50m1	HasZ-100m1
n	9	33	11	20
SiO_2	35.67 (387)	38.34 (288)	36.07 (215)	37.94 (238)
Al_2O_3	9.52 (147)	10.20 (82)	12.16 (185)	9.33 (121)
FeO	22.34 (118)	21.84 (153)	27.82 (180)	28.51 (134)
Fe_2O_3	10.54 (104)	10.90 (118)	4.08 (138)	4.68 (84)
CaO	9.56 (96)	9.93 (65)	10.38 (47)	9.93 (47)
Na_2O	0	0	0	0
K_2O	2.35 (42)	2.10 (27)	2.77 (25)	2.87 (29)
Cl	1.54 (26)	1.86 (22)	2.68 (36)	2.85 (32)
H_2O*	0.64 (31)	0.32 (24)	1.07 (12)	0.80 (14)
Total	90.47 (675)	94.08 (515)	95.56 (368)	95.64 (400)
Site assignments				
^{T}Si	6.38 (25)	6.57 (19)	6.17 (22)	6.55 (25)
^{T}Al	1.61 (24)	1.43 (19)	1.83 (22)	1.45 (25)
$^{T}Fe^{3+}$	0.01 (2)	0.00 (0)	0.00 (0)	0.00 (0)
Sum T	8	8	8	8
^{C}Al	0.39 (28)	0.64 (17)	0.62 (20)	0.44 (12)
$^{C}Fe^{3+}$	1.38 (9)	1.41 (5)	0.53 (17)	0.61 (9)
$^{C}Fe^{2+}$	3.23 (19)	2.96 (12)	3.85 (20)	3.95 (7)
Sum C	5	5	5	5
^{B}Fe	0.17 (6)	0.18 (8)	0.13 (7)	0.17 (6)
^{B}Ca	1.83 (6)	1.82 (8)	1.89 (7)	1.83 (6)
Sum-B	2	2	2	2
^{A}Na	0	0	0	0
^{A}K	0.53 (7)	0.46 (6)	0.60 (6)	0.63 (6)
^{A}Ca	0.01 (1)	0.01 (0)	0.04 (4)	0.01 (0)
Sum-A	0.54 (7)	0.47 (6)	0.64 (7)	0.64 (6)
Cations	15.54 (7)	15.46 (6)	15.64 (7)	15.64 (6)
Cl	0.47 (7)	0.54 (7)	0.78 (11)	0.84 (9)
OH	0.85 (42)	0.37 (24)	1.22 (11)	0.92 (16)
Anions	1.32 (42)	0.91 (27)	2.00 (1)	1.76 (21)
Fe^{3+}/Fe^{total}	0.289 (14)	0.310 (16)	0.116 (6)	0.128 (6)

Note: Analyses reported as weight percent of the oxides and cations per 24 O+Cl+OH atoms of the average of *n* electron microprobe analyses. The ferric iron proportion was determined via Mössbauer analysis.

*H_2O was calculated by minimizing ^{A}Ca and barring K from the B site. Uncertainties (1σ) in the last digit are shown in parentheses.

This is the peer-reviewed, final accepted version for American Mineralogist, published by the Mineralogical Society of America.
The published version is subject to change. Cite as Authors (Year) Title. American Mineralogist, in press.
DOI: https://doi.org/10.2138/am-2023-9083. http://www.minsocam.org/

754 **Table 3b.** Compositions of amphiboles synthesized at the conditions listed in Table 1 for which
755 ferric iron was estimated as discussed in the text.
756

Exp Name	ZN-1m1	ZN-3m1	ZN-12m1	ZN-50m1
n	11	14	14	10
SiO_2	35.59 (202)	34.86 (281)	35.69 (264)	34.90 (267)
Al_2O_3	8.94 (90)	9.56 (92)	9.58 (107)	10.46 (169)
FeO	27.42 (146)	27.07 (248)	25.83 (220)	23.94 (563)
Fe_2O_3	5.22 (104)	6.46 (166)	8.96 (254)	10.19 (606)
CaO	9.26 (68)	9.11 (82)	9.09 (57)	9.46 (94)
Na_2O	2.14 (18)	1.80 (24)	1.48 (24)	2.00 (26)
K_2O	0	0	0	0
Cl	0.21 (3)	0.50 (6)	1.05 (10)	2.79 (43)
H_2O*	1.39 (19)	1.47 (18)	1.18 (21)	0.53 (69)
Total	88.25 (455)	88.72 (611)	90.78 (473)	92.72 (642)
Site assignments				
^{T}Si	6.44 (8)	6.27 (11)	6.29 (18)	6.16 (9)
^{T}Al	1.56 (8)	1.73 (10)	1.68 (17)	1.84 (8)
$^{T}Fe^{3+}$	0.00 (0)	0.00 (0)	0.03 (7)	0.00 (0)
Sum T	8	8	8	8
^{C}Al	0.35 (17)	0.30 (16)	0.31 (24)	0.33 (33)
$^{C}Fe^{3+}$	0.72 (7)	0.88 (23)	1.16 (28)	1.35 (16)
$^{C}Fe^{2+}$	3.93 (12)	3.82 (11)	3.53 (12)	3.32 (21)
Sum C	5	5	5	5
^{B}Fe	0.21 (5)	0.25 (7)	0.29 (10)	0.22 (11)
^{B}Ca	1.79 (5)	1.75 (7)	1.71 (10)	1.78 (11)
Sum-B	2	2	2	2
^{A}Na	0.75 (6)	0.63 (4)	0.51 (7)	0.69 (6)
^{A}K	0	0	0	0
^{A}Ca	0.00 (0)	0.01 (0)	0.01 (0)	0.01 (4)
Sum-A	0.75 (6)	0.64 (4)	0.52 (7)	0.70 (6)
Cations	15.75 (6)	15.63 (4)	15.51 (7)	15.69 (4)
Cl	0.06 (1)	0.15 (2)	0.31 (3)	0.83 (10)
OH	1.67 (19)	1.76 (10)	1.41 (21)	0.63 (21)
Anions	1.74 (19)	1.91 (10)	1.72 (23)	1.46 (26)
Fe^{3+}/Fe^{total}	0.148 (12)	0.178 (14)	0.234 (19)	0.276 (93)

757
758

This is the peer-reviewed, final accepted version for American Mineralogist, published by the Mineralogical Society of America.
The published version is subject to change. Cite as Authors (Year) Title. American Mineralogist, in press.
DOI: https://doi.org/10.2138/am-2023-9083. http://www.minsocam.org/

759

760 **Table 3b.** (continued)

Exp Name	KN0.25-1m1	KN0.25-3m1	KN0.25-12m1	KN0.25-50m1	KN0.25-100m1
n	18	13	17	13	9
SiO_2	36.38 (305)	35.50 (378)	36.82 (208)	37.58 (214)	34.49 (366)
Al_2O_3	10.20 (181)	10.56 (108)	10.21 (105)	10.64 (96)	9.75 (141)
FeO	27.30 (160)	26.42 (262)	25.76 (206)	25.79 (553)	23.95 (570)
Fe_2O_3	5.27 (85)	6.47 (136)	9.11 (181)	8.29 (612)	10.07 (607)
CaO	9.40 (150)	9.53 (93)	9.32 (101)	10.16 (90)	9.13 (96)
Na_2O	1.84 (44)	1.64 (27)	1.30 (29)	1.53 (29)	1.55 (38)
K_2O	1.03 (13)	0.68 (7)	0.54 (8)	0.72 (10)	0.63 (14)
Cl	0.23 (4)	0.53 (7)	1.12 (20)	2.75 (27)	2.66 (38)
H_2O*	1.25 (26)	1.32 (20)	1.04 (37)	0.60 (74)	0.54 (75)
Total	91.12 (752)	90.68 (765)	93.27 (318)	96.63 (298)	91.22 (586)
Site assignments					
^{T}Si	6.40 (20)	6.25 (18)	6.33 (17)	6.35 (21)	6.20 (36)
^{T}Al	1.60 (20)	1.75 (16)	1.67 (17)	1.65 (20)	1.80 (35)
$^{T}Fe^{3+}$	0.00 (0)	0.00 (0)	0.00 (0)	0.00 (0)	0.00 (0)
Sum T	8	8	8	8	8
^{C}Al	0.50 (17)	0.44 (23)	0.40 (25)	0.47 (32)	0.27 (18)
$^{C}Fe^{3+}$	0.71 (4)	0.86 (14)	1.17 (10)	1.05 (17)	1.37 (20)
$^{C}Fe^{2+}$	3.79 (14)	3.69 (15)	3.43 (18)	3.48 (19)	3.36 (14)
Sum C	5	5	5	5	5
^{B}Fe	0.24 (19)	0.20 (15)	0.29 (15)	0.16 (17)	0.24 (20)
^{B}Ca	1.76 (19)	1.80 (15)	1.71 (15)	1.83 (17)	1.76 (20)
Sum-B	2	2	2	2	2
^{A}Na	0.62 (13)	0.56 (8)	0.44 (10)	0.50 (9)	0.54 (14)
^{A}K	0.23 (2)	0.15 (2)	0.12 (2)	0.16 (2)	0.15 (3)
^{A}Ca	0.00 (0)	0.00 (6)	0.01 (0)	0.01 (0)	0.01 (3)
Sum-A	0.85 (13)	0.81 (10)	0.57 (11)	0.67 (9)	0.70 (14)
Cations	15.86 (12)	15.72 (11)	15.56 (11)	15.66 (9)	15.69 (13)
Cl	0.07 (1)	0.16 (2)	0.33 (6)	0.79 (8)	0.81 (10)
OH	1.46 (28)	1.56 (24)	1.21 (35)	0.68 (34)	0.66 (42)
Anions	1.53 (28)	1.72 (25)	1.54 (33)	1.47 (38)	1.47 (35)
Fe^{3+}/Fe^{total}	0.150 (12)	0.181 (15)	0.239 (26)	0.224 (95)	0.275 (93)

761

762

This is the peer-reviewed, final accepted version for American Mineralogist, published by the Mineralogical Society of America.
The published version is subject to change. Cite as Authors (Year) Title. American Mineralogist, in press.
DOI: https://doi.org/10.2138/am-2023-9083. http://www.minsocam.org/

763 **Table 3b.** (continued)

Exp Name	KN0.5-1m1	KN0.5-3m1	KN0.5-12m1	KN0.5-50m1	KN0.5-100m1
n	17	22	19	16	13
SiO_2	35.02 (146)	35.69 (175)	36.31 (191)	35.91 (154)	34.35 (221)
Al_2O_3	11.52 (61)	10.83 (117)	11.23 (284)	11.69 (157)	10.15 (94)
FeO	26.55 (110)	25.16 (139)	25.02 (181)	24.27 (562)	24.12 (530)
Fe_2O_3	5.24 (79)	6.53 (97)	9.21 (159)	10.28 (622)	8.62 (579)
CaO	10.20 (48)	9.89 (40)	9.51 (45)	9.96 (61)	9.45 (78)
Na_2O	1.18 (7)	0.90 (9)	0.79 (7)	1.00 (6)	1.16 (21)
K_2O	1.76 (17)	1.44 (9)	1.17 (12)	1.62 (11)	1.69 (20)
Cl	0.26 (2)	0.61 (5)	1.19 (15)	2.76 (31)	3.43 (36)
H_2O*	1.52 (12)	1.24 (15)	1.07 (22)	0.59 (74)	0.34 (66)
Total	91.20 (306)	90.39 (346)	93.50 (286)	96.46 (136)	92.10 (401)
Site assignments					
^{T}Si	6.13 (9)	6.30 (15)	6.22 (26)	6.10 (24)	6.20 (17)
^{T}Al	1.87 (9)	1.70 (15)	1.78 (26)	1.90 (24)	1.80 (17)
$^{T}Fe^{3+}$	0.00 (0)	0.00 (0)	0.00 (0)	0.00 (0)	0.00 (0)
Sum T	8	8	8	8	8
^{C}Al	0.51 (6)	0.55 (13)	0.48 (30)	0.43 (14)	0.36 (14)
$^{C}Fe^{3+}$	0.70 (1)	0.87 (2)	1.18 (9)	1.31 (5)	1.17 (9)
$^{C}Fe^{2+}$	3.79 (5)	3.58 (11)	3.34 (23)	3.25 (12)	3.47 (12)
Sum C	5	5	5	5	5
^{B}Fe	0.09 (4)	0.13 (3)	0.26 (5)	0.19 (10)	0.18 (10)
^{B}Ca	1.91 (4)	1.87 (3)	1.74 (5)	1.81 (10)	1.82 (10)
Sum-B	2	2	2	2	2
^{A}Na	0.40 (2)	0.31 (3)	0.26 (2)	0.33 (2)	0.41 (8)
^{A}K	0.39 (4)	0.32 (2)	0.26 (2)	0.35 (3)	0.39 (4)
^{A}Ca	0.01 (1)	0.00 (0)	0.01 (0)	0.01 (1)	0.00 (0)
Sum-A	0.80 (4)	0.63 (3)	0.53 (3)	0.69 (4)	0.80 (9)
Cations	15.80 (5)	15.64 (3)	15.52 (3)	15.69 (4)	15.80 (7)
Cl	0.08 (0)	0.18 (2)	0.35 (5)	0.79 (9)	1.05 (10)
OH	1.77 (8)	1.46 (13)	1.25 (17)	0.67 (27)	0.42 (15)
Anions	1.85 (8)	1.64 (14)	1.60 (19)	1.46 (26)	1.46 (19)
Fe^{3+}/Fe^{total}	0.153 (12)	0.189 (14)	0.246 (23)	0.276 (98)	0.243 (91)

764

765

This is the peer-reviewed, final accepted version for American Mineralogist, published by the Mineralogical Society of America.
The published version is subject to change. Cite as Authors (Year) Title. American Mineralogist, in press.
DOI: https://doi.org/10.2138/am-2023-9083. http://www.minsocam.org/

Table 3b. (continued)

Exp Name	KN0.75-1m1	KN0.75-3m1	KN0.75-12m1	KN0.75-50m1	KN0.75-100m1
n	13	19	16	18	19
SiO_2	34.23 (276)	35.45 (188)	36.92 (240)	35.47 (181)	34.91 (170)
Al_2O_3	11.03 (101)	11.01 (75)	10.46 (74)	11.34 (225)	10.52 (100)
FeO	25.34 (151)	25.44 (156)	25.31 (166)	23.88 (575)	23.47 (548)
Fe_2O_3	5.45 (89)	7.02 (103)	9.50 (153)	9.85 (631)	11.42 (606)
CaO	9.53 (141)	10.18 (61)	9.84 (41)	10.07 (33)	10.12 (60)
Na_2O	0.61 (12)	0.50 (3)	0.42 (3)	0.51 (5)	0.52 (4)
K_2O	2.54 (43)	2.14 (13)	1.74 (23)	2.46 (13)	2.63 (13)
Cl	0.35 (4)	0.71 (6)	1.25 (14)	3.48 (22)	3.66 (15)
H_2O*	1.30 (18)	1.34 (20)	1.07 (23)	0.39 (72)	0.33 (69)
Total	88.53 (578)	91.75 (446)	94.48 (307)	96.07 (257)	96.11 (271)
Site assignments					
^{T}Si	6.20 (12)	6.19 (11)	6.28 (21)	6.12 (23)	6.06 (17)
^{T}Al	1.80 (12)	1.81 (11)	1.72 (21)	1.88 (23)	1.94 (17)
$^{T}Fe^{3+}$	0.00 (0)	0.00 (0)	0.00 (0)	0.00 (0)	0.00 (0)
Sum T	8	8	8	8	8
^{C}Al	0.56 (12)	0.46 (11)	0.39 (15)	0.42 (24)	0.22 (13)
$^{C}Fe^{3+}$	0.75 (4)	0.92 (3)	1.21 (8)	1.28 (6)	1.49 (8)
$^{C}Fe^{2+}$	3.69 (11)	3.62 (9)	3.41 (12)	3.30 (20)	3.29 (8)
Sum C	5	5	5	5	5
^{B}Fe	0.16 (19)	0.10 (4)	0.21 (6)	0.14 (6)	0.12 (8)
^{B}Ca	1.84 (20)	1.90 (4)	1.79 (6)	1.86 (6)	1.88 (8)
Sum-B	2	2	2	2	2
^{A}Na	0.21 (5)	0.17 (1)	0.14 (1)	0.17 (2)	0.17 (1)
^{A}K	0.59 (13)	0.48 (2)	0.38 (6)	0.54 (3)	0.58 (2)
^{A}Ca	0.01 (1)	0.01 (0)	0.00 (0)	0.00 (0)	0.00 (0)
Sum-A	0.81 (14)	0.66 (2)	0.52 (6)	0.71 (4)	0.75 (3)
Cations	15.81 (10)	15.65 (2)	15.52 (5)	15.72 (4)	15.76 (3)
Cl	0.11 (1)	0.21 (2)	0.36 (5)	1.02 (8)	1.08 (5)
OH	1.57 (16)	1.56 (17)	1.23 (20)	0.45 (12)	0.38 (15)
Anions	1.68 (17)	1.77 (18)	1.59 (23)	1.46 (17)	1.46 (19)
Fe^{3+}/Fe^{total}	0.164 (13)	0.199 (15)	0.250 (22)	0.271 (100)	0.304 (95)

Note: Analyses reported as weight percent of the oxides and cations per 24 O+Cl+OH atoms of the average of *n* electron microprobe analyses.
*H_2O was estimated by minimizing ^{A}Ca and barring K from the B site. Uncertainties (1σ) in the last digit are shown in parentheses.

773
774 **Figure 1.**
775

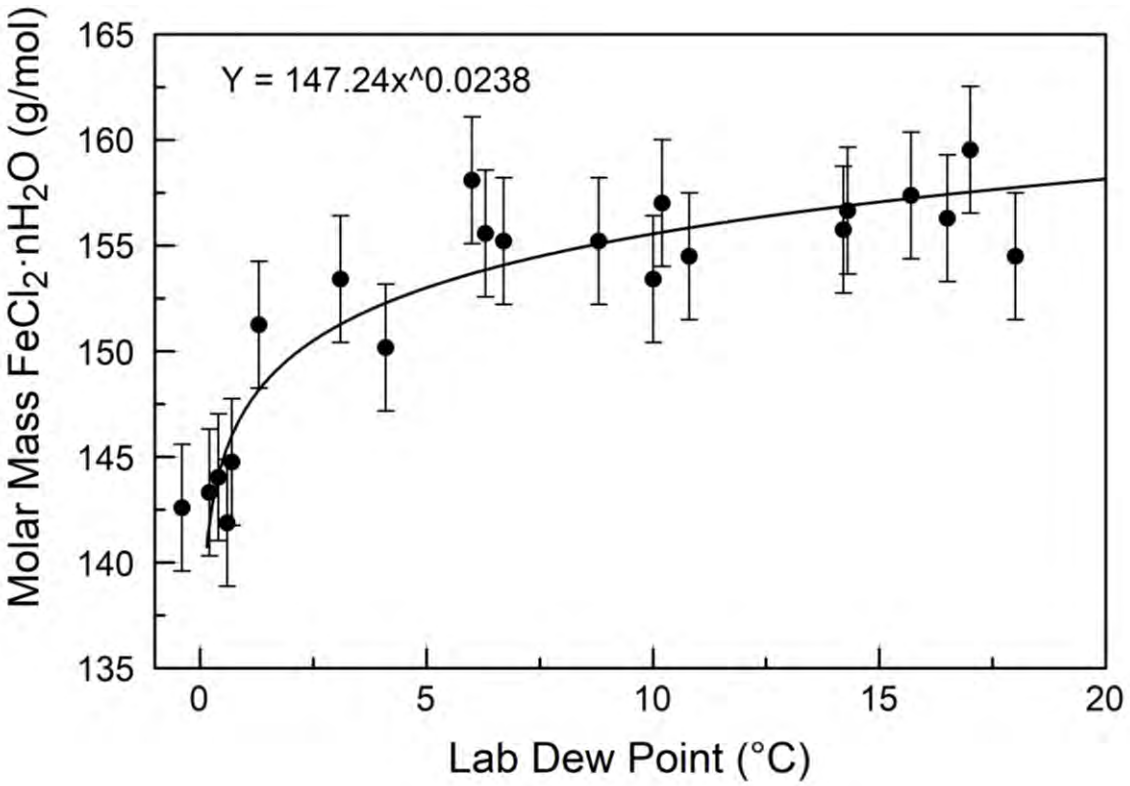

776
777
778

779
780 **Figure 2**

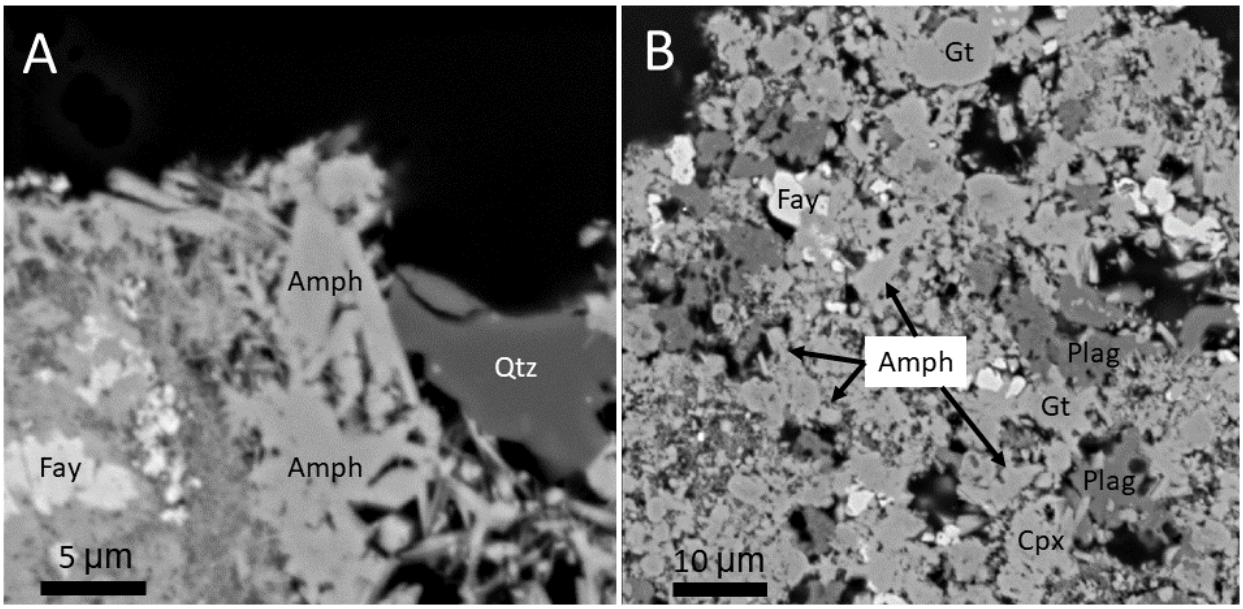

781
782
783

Figure 3.

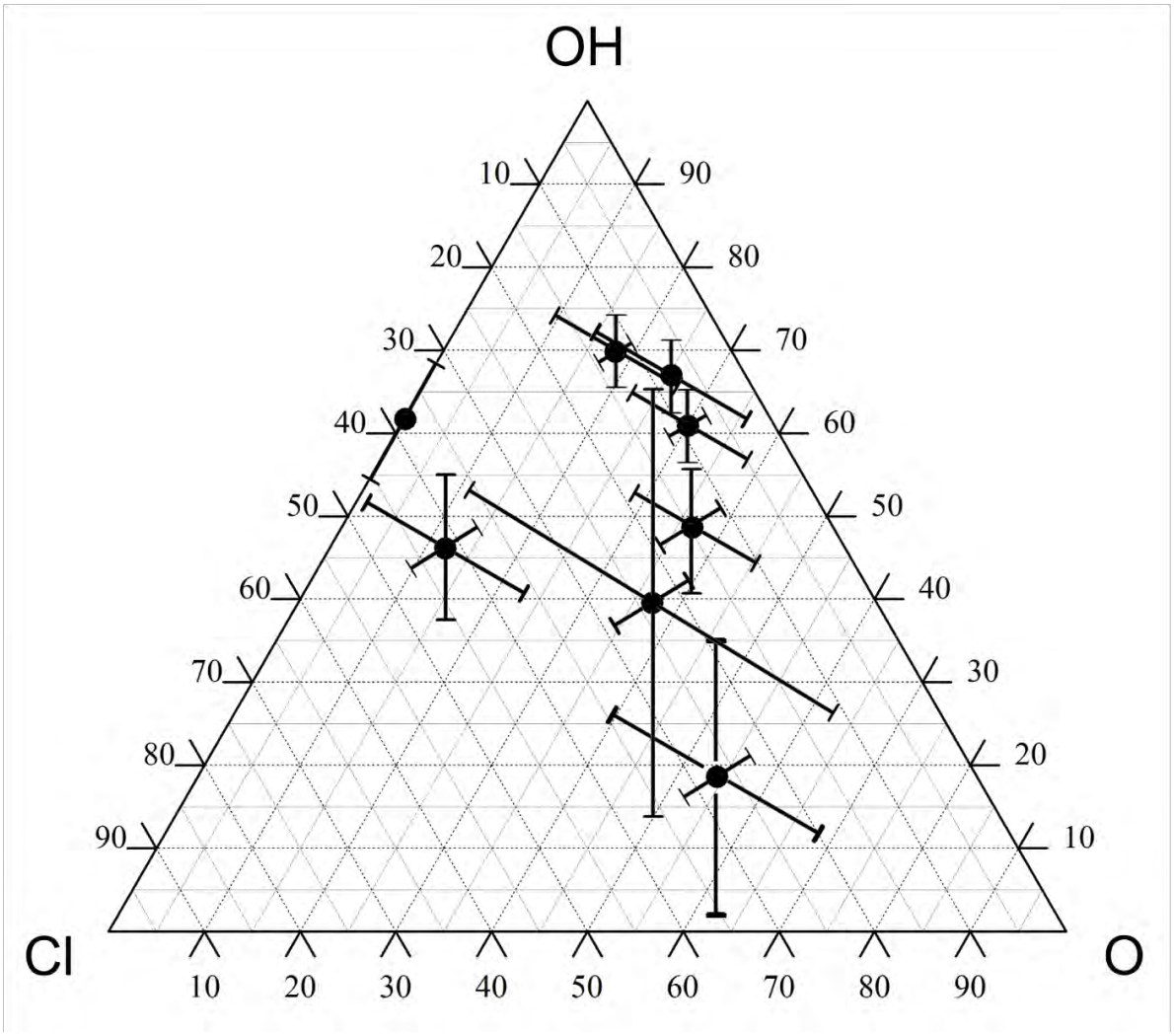

789
790 **Figure 4.**
791

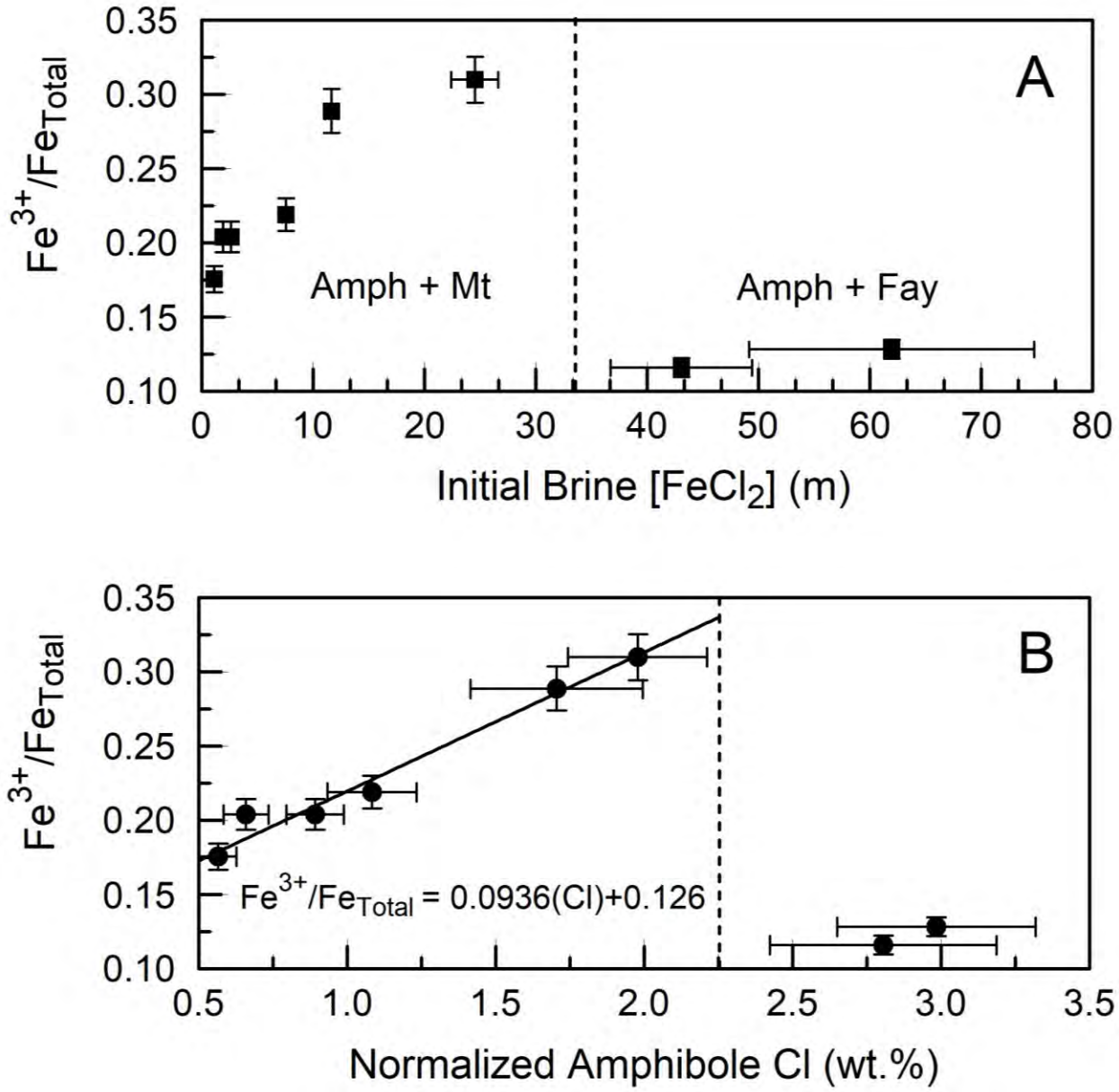

792
793

794

Figure 5.

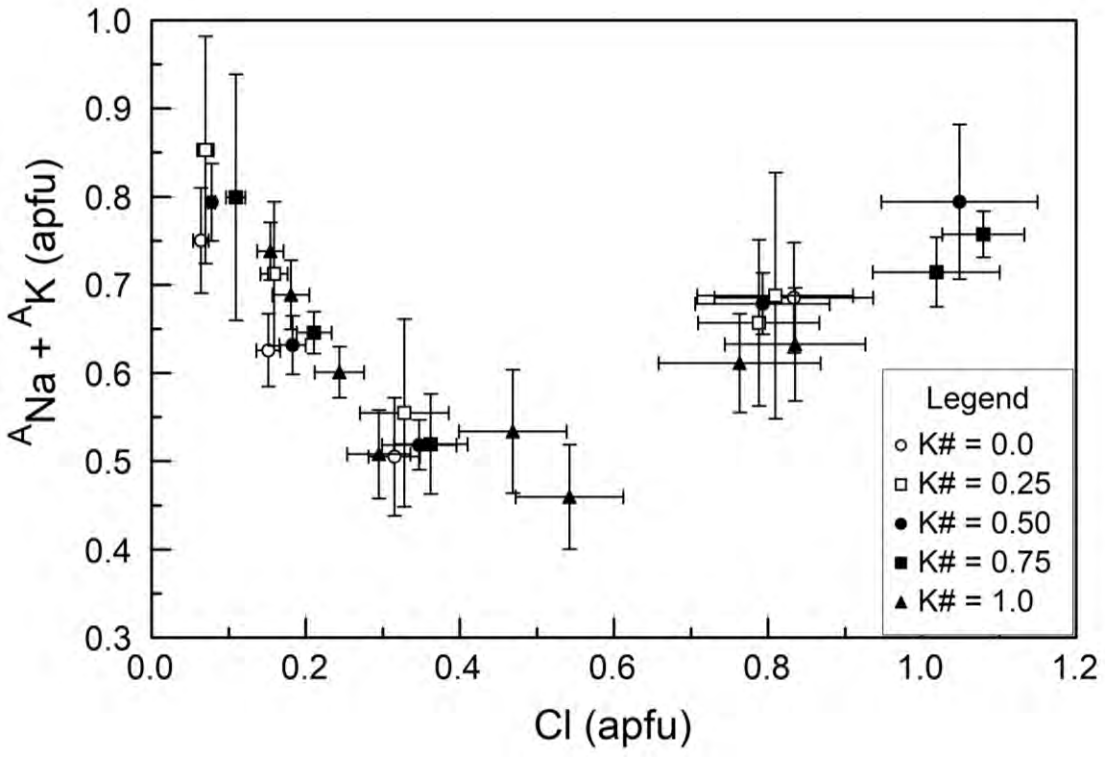

800

801 **Figure 6.**

802

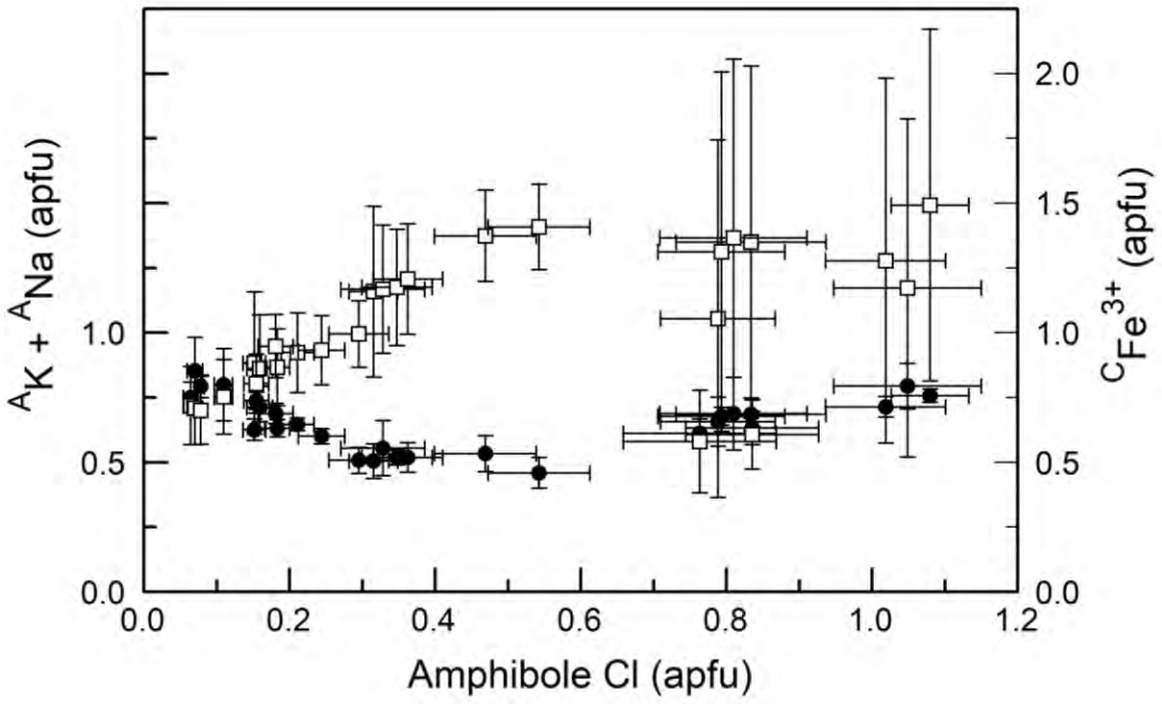

803

804

805

806 **Figure 7.**

807

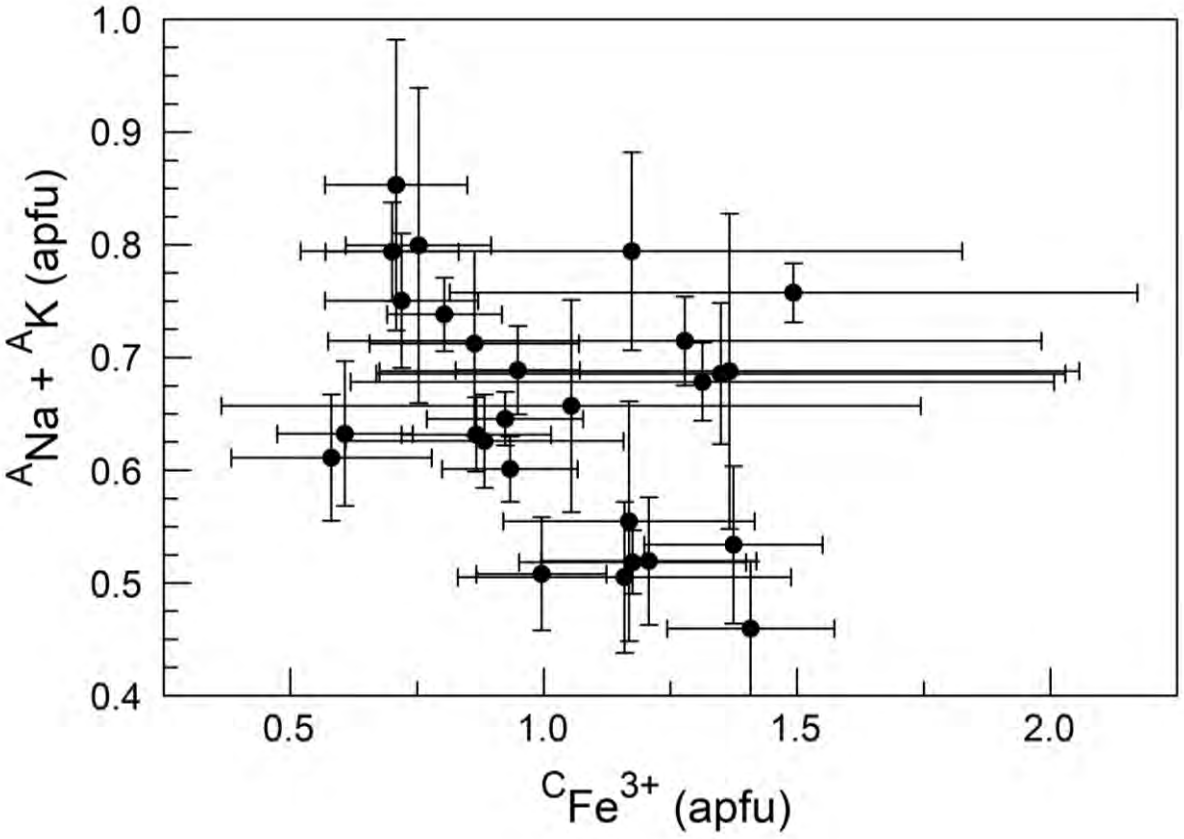

808

809

810

811

812

813

814

815

816

817

818 **Figure 8.**

819

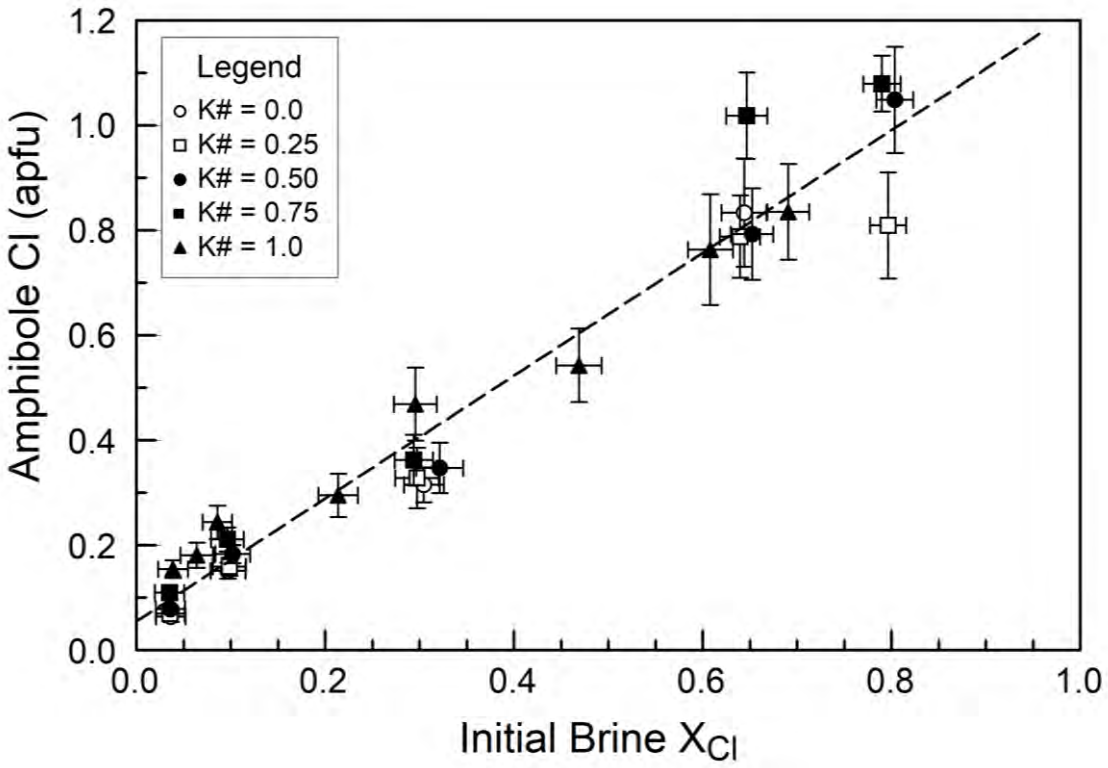

820

821

822

823

824

825

826

827

828

829

830

This is the peer-reviewed, final accepted version for American Mineralogist, published by the Mineralogical Society of America.
The published version is subject to change. Cite as Authors (Year) Title. American Mineralogist, in press.
DOI: https://doi.org/10.2138/am-2023-9083. http://www.minsocam.org/

831

832 **Figure 9.**

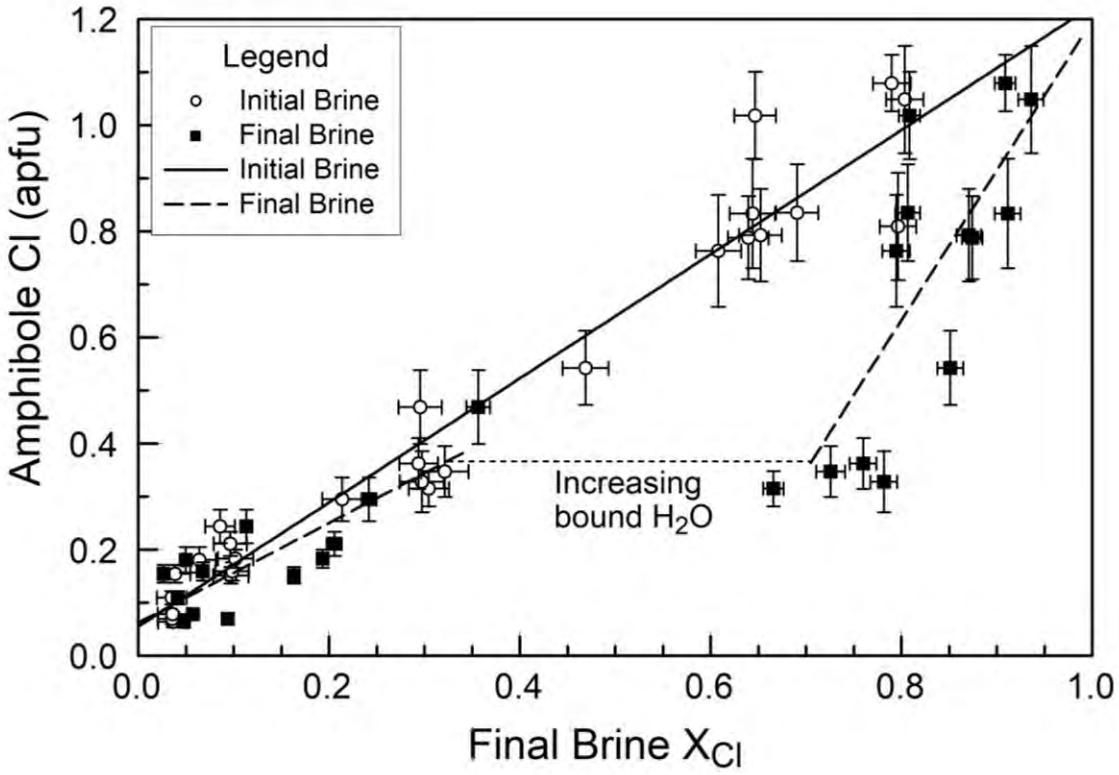

833

834

835

This is the peer-reviewed, final accepted version for American Mineralogist, published by the Mineralogical Society of America.
The published version is subject to change. Cite as Authors (Year) Title. American Mineralogist, in press.
DOI: https://doi.org/10.2138/am-2023-9083. http://www.minsocam.org/

836
837 **Figure 10.**
838

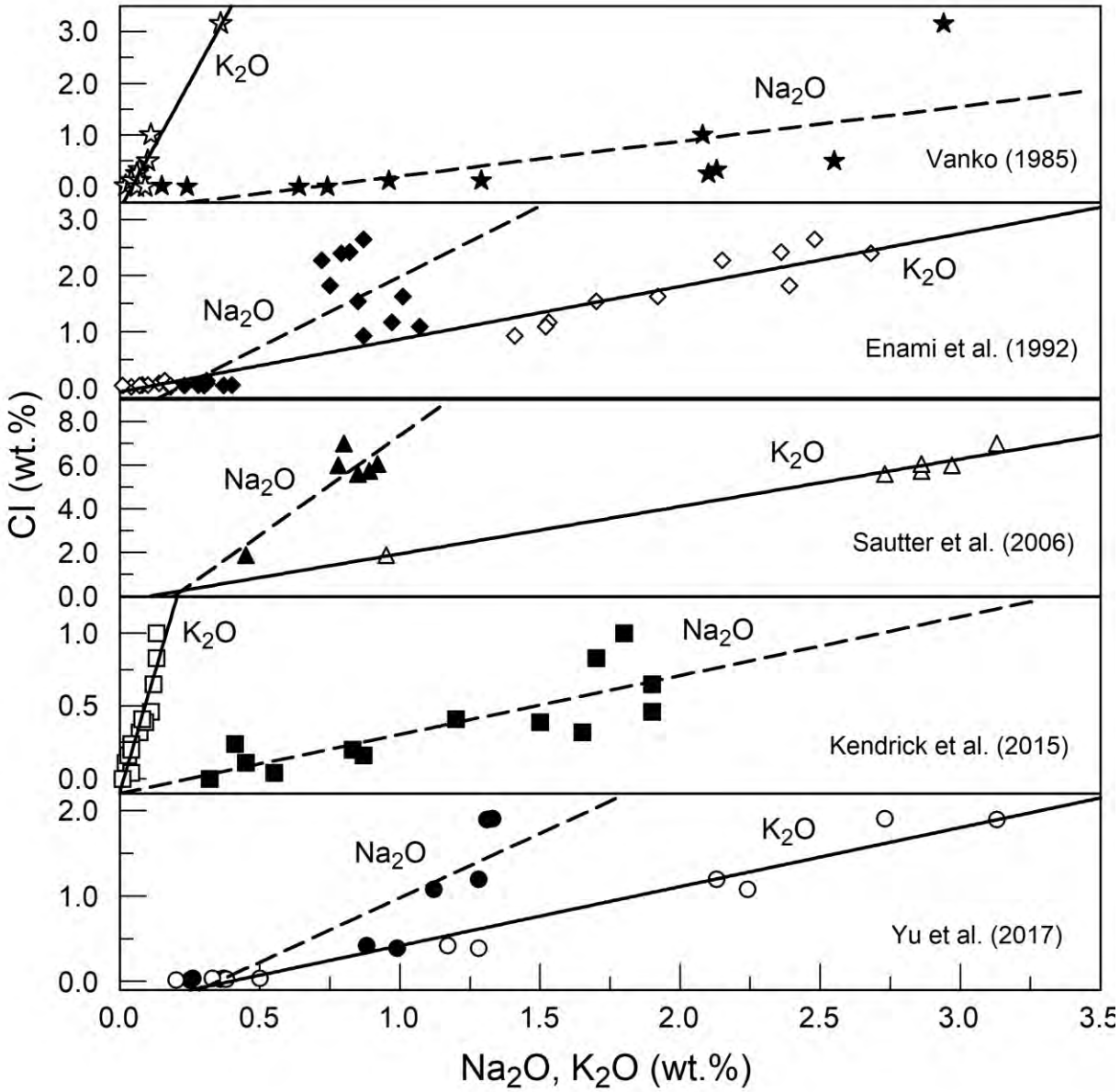

839
840
841

842

843
844 **Figure 11.**
845

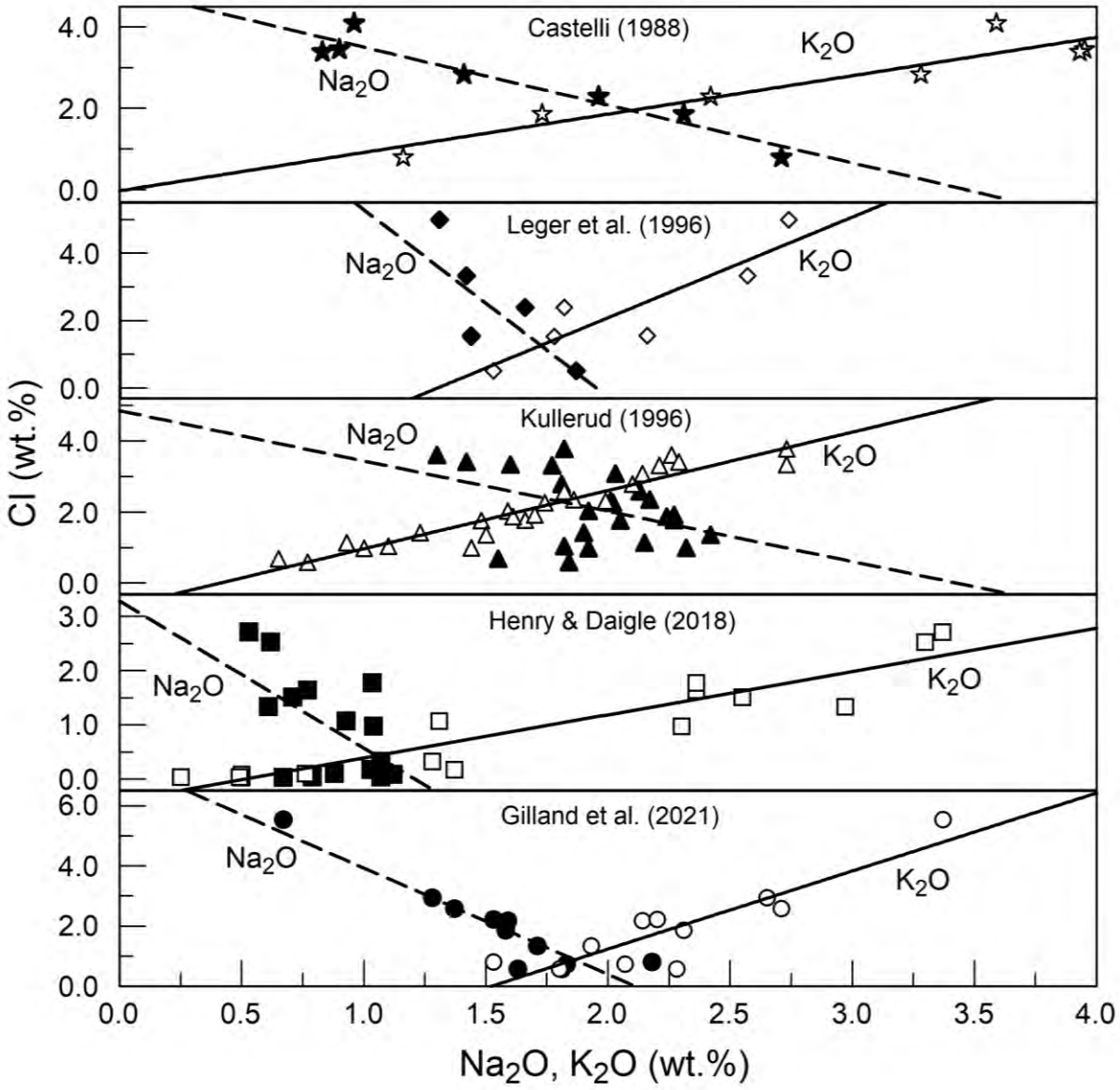

846
847

848

849
850 Figure Captions
851
852 **Figure 1.** Lab dewpoint vs molar mass of $FeCl_2 \cdot nH_2O$. Molar mass is in units of grams per mole.
853 For reference, the molar mass of anhydrous $FeCl_2$ is 126.75 g/mole.
854
855 **Figure 2.** Representative back-scattered electron images of amphibole synthesis products made
856 in Jenkins (2019) at conditions similar to those used in this study. (a) Synthetic potassic-chloro-
857 hastingsite with coexisting fayalite and quartz made at 700°C and 4.2 kbar for 116 h at fO_2 of -
858 1.9 ΔNi-NiO from a nominally dry mixture with K# of 1.0. (b) Synthetic chloro-hastingsite
859 with coexisting fayalite, clinopyroxene, plagioclase, and garnet (Gt) made at 700°C and 4.3 kbar
860 for 168 h at fO_2 of -2.0 ΔNi-NiO from a nominally dry mixture with K# of 0.0. Abbreviations as
861 in Table 1.
862
863 **Figure 3.** Percentages of OH, Cl, and O on the *O*(3) sites of Mössbauer-analyzed amphiboles.
864 OH was determined via charge balance, as described in the text; the remainder of the *O*(3) sites
865 were filled with oxygen.
866
867 **Figure 4. (a)** Ferric iron fraction vs initial brine $FeCl_2$ concentration. **(b)** Amphibole Cl content
868 (wt.%) vs ferric iron fraction. The solid line is a Deming regression to the data. The dashed line
869 represents the magnetite - fayalite transition between $FeCl_2$ brine concentrations of 24m and
870 50m. Ferric iron fraction was determined via Mössbauer spectroscopy with an assumed
871 uncertainty of 5%. Abbreviations: Mt = magnetite, Fay = fayalite.
872
873 **Figure 5.** Total *A*-cations vs Cl. Different symbols represent the various K# series as indicated in
874 the legend.
875
876 **Figure 6.** Total *A*-site cations and octahedral Fe^{3+} vs amphibole Cl. Closed circles represent total
877 *A*-site cations and open squares represent octahedral ferric iron.
878
879 **Figure 7.** Total *A*-site cations vs octahedral Fe^{3+}.
880
881 **Figure 8.** Initial brine X_{Cl} (mole fraction Cl) vs amphibole Cl. Dashed line is a linear regression
882 to the data (Y=1.170x+0.0549). Note: these concentrations represent that of the brine at the
883 beginning of treatment at P and T.
884
885 **Figure 9.** Comparison of $FeCl_2$ brines calculated with initial vs final water content.
886
887 **Figure 10.** Review of natural amphiboles showing a positive correlation between both Na-Cl and
888 K-Cl. Solid symbols represent Na_2O, open symbols represent K_2O. Circles: Yu et al. (2017);
889 squares: Kendrick et al. (2015); triangles: Sautter et al. (2006); diamonds: Enami et al. (1992);
890 stars: Vanko (1985). Lines are linear regressions to the data.
891
892 **Figure 11.** Review of natural amphiboles showing a positive correlation between K-Cl and a
893 negative correlation between Na-Cl. Solid symbols represent Na_2O, open symbols represent
894 K_2O. Circles: Gilland et al. (2021); squares: Henry and Daigle (2018); triangles: Kullerud

(1996); diamonds: Legér et al. (1996); stars: Castelli (1988). Lines are linear regressions to the data.

Supplemental Figure 1. A portion of the monoclinic (C2/m) amphibole structure projected onto the (100) labeled with the sites in the general mineral formula $A_{0\text{-}1}B_2C_5T_8O_{22}W_2$ in the lower half of the diagram, and the specific crystallographic sites, excluding most of the oxygens, labeled in the upper portion. Cl, OH, and O reside at the O(3) site.